



Understanding of topological mode and skin mode morphing in 1D and 2D non-Hermitian resonance-based meta-lattices

Qian Wu ^a, Shaoyun Wang ^a, Honghua Qian ^a, Yanzheng Wang ^a, Guoliang Huang ^{b,*}

^a Department of Mechanical and Aerospace Engineering, University of Missouri, Columbia, Missouri 65211, USA

^b Department of Mechanics and Engineering Science, College of Engineering, Peking University, Beijing 100871, PR China

ARTICLE INFO

Keywords:

Non-Hermitian system
Local resonance
Topological mode
Skin mode
Active control

ABSTRACT

Recent advances have demonstrated that the non-Hermitian skin effect (NHSE), induced by system non-Hermiticity, can manipulate the localization of in-gap topological edge modes (TEMs) within mechanical topological insulators. This study introduces a straightforward analytical framework to elucidate the competition between NHSE and TEM localization in a classical mechanical meta-lattice, highlighting its impact on the dynamic behavior of TEMs within separate Bragg scattering band gaps (BSBGs). We propose a 1D non-Hermitian meta-lattice featuring a locally resonant system with active feedback control, characterized by a real-valued transfer function. This local resonance creates two separate BSBGs, each hosting a TEM defined by non-Hermitian bulk-edge correspondence. Our theoretical and numerical analyses reveal that the NHSE, with its asymmetric localization within the two BSBGs, can shift the localization of TEMs in distinct ways. This leads to an asymmetric phase transition, wherein one TEM can be delocalized and relocalized by tuning the transfer function, while the other maintains its initial localization. Moreover, we extend the mechanism of 1D asymmetric TEM delocalization to the non-Hermitian morphing of TEMs, showcasing notable examples such as temporal and spatial topological wave pumping with space- and time-dependent transfer functions in 1D time-varying and 2D stacked meta-lattices. This research bridges a gap between non-Hermitian mechanical constructs and their potential applications in classical mechanics, reinterpreting known topological wave control in 1D and uncovering new mechanisms in 2D.

1. Introduction

Topological insulators represent new phases of matter whose properties are derived from a number of qualitative yet robust topological invariants rather than specific geometric features or constitutive parameters. These topological invariants, derived from Bloch band theory, indicate the appearance of topological edge modes (TEMs) according to the celebrated bulk-edge correspondence (Chiu et al., 2016). The salient feature of the TEMs is that they are localized along edges and interfaces with negligible scattering and losses induced by the presence of specific varieties of defects compatible with their topological class. Because the governing equations for different physical systems can be formulated as eigenvalue problems (Arfken et al., 2011), the idea of band topology has been lately extended into classical wave areas (Ni et al., 2023; Ma et al., 2019), such as photonic (Lu et al., 2014), acoustic (He et al., 2016), and elastic waves (Fan et al., 2019), although it was discovered initially in quantum systems for electrons (Klitzing et al., 1980; Thouless et al., 1982).

* Corresponding author.

E-mail address: guohuang@pku.edu.cn (G. Huang).

On the other hand, non-Hermitian physics has been attracting considerable interest where the conservation of energy does not hold by integrating active elements into passive systems for controllable energetic exchanges with the surroundings, leading to complex spectra. Specifically, non-Hermitian frequency bands are extended from real to complex domains. Owing to the nonorthogonal nature of eigenstates, the non-Hermiticity challenges the conventional understanding of the bulk-edge correspondence. To describe the topological aspects of non-Hermitian topological systems accurately, the generalized Brillouin zone approach is often employed with the biorthogonality of eigenvectors, extending the traditional notion of Brillouin zone from Hermitian to non-Hermitian systems and formulating an unconventional non-Bloch bulk-edge correspondence (Kunst et al., 2018; Yang et al., 2020; Ghatak et al., 2020). Non-Hermitian skin effect (NHSE) has been recognized as one of the seminal findings in non-Hermitian systems (Ashida et al., 2020; Bergholtz et al., 2021). Due to NHSE, eigenstates of a finite non-Hermitian system tend to exponentially pile up at its boundaries. It is noteworthy that NHSE itself has a topological origin, arising from a point-gapped spectrum with spectral winding on the complex energy plane (Okuma et al., 2020). As NHSE has been observed in various experiments, the exploration of new facets in topological non-Hermitian systems has garnered significant interest. It should be mentioned that although both NHSE and TEMs feature eigenstates localized towards system boundaries, their emergence and direction of localization are governed by different topological invariants.

Recently, the intersection of topological and non-Hermitian physics has been the focus of extensive numerical and experimental studies, providing deeper insights into the fundamental nature of topological matter and non-Hermitian energy transport (Okuma et al., 2020; Leykam et al., 2017; He and Chien, 2020; Gong et al., 2018; Ding et al., 2022). This growing interest is driven in part by the ability to introduce controllable non-Hermitian elements, which offer increased flexibility in manipulating topological phases and expanding their potential applications. In recent years, it has been shown that the interplay between these elements can result in the delocalization of TEMs, with topological invariants and geometric factors playing key roles in this behavior. However, these TEM delocalization behaviors have primarily been observed in a single topologically nontrivial Bragg scattering band gap (BSBG) using tight-binding models, which may not be directly transferable to continuous mechanical systems. To bridge this gap and uncover richer TEM delocalization phenomena, including multiband characteristics, a classical mechanics-based approach is necessary to enrich the interactions between TEMs and NHSE.

In this work, we introduce a locally resonant non-Hermitian topological meta-lattice, featuring a sensing-actuating feedback loop controlled by a programmable transfer function. The local resonance generates two topologically nontrivial BSBGs with enriched dynamics for the NHSE (Huang and Sun, 2009; Wu et al., 2023b). Our focus is to demonstrate asymmetric TEM delocalization, driven by local resonance, which reshapes the competitive interactions between NHSE and TEMs within the two BSBGs in the framework of classical mechanics. Notably, unlike previous studies (Wang et al., 2022b; Ghatak et al., 2020; Zhu et al., 2021), the asymmetric TEM delocalization explored here arises within either of the BSBGs, due to the opposing localization effects of NHSE, which selectively counterbalance the inherent localization of certain TEMs. Additionally, we find that the control strengths required for this asymmetric TEM delocalization in finite non-Hermitian lattices with open boundary conditions (OBCs) differ from those required for the emergence of exceptional points in periodic lattices with periodic boundary conditions (PBCs). Thanks to the spring-mass modeling, we can quantitatively analyze how mechanical system parameters influence the asymmetric TEM delocalization and validate these findings through finite-difference simulations in 1D systems. We also explore the properties of multiple phase transitions featuring distinct TEM delocalization behaviors, an area that remains largely unexplored within classical mechanics. Furthermore, we extend the concept of asymmetric TEM delocalization to the 1D temporal and 2D spatial morphing of TEMs by considering time- and space-dependent transfer functions in 1D time-varying and 2D stacked meta-lattices. Importantly, all 1D and 2D meta-lattices proposed can be physically realized using structured beams and plates, thanks to the classical spring-mass framework, while the active feedback control facilitated by sensing-actuating loops can be readily implemented using piezoelectric materials shunted with external circuits (Wu et al., 2022, 2023a; Chen et al., 2021b; Yi et al., 2022). This study represents the first adaptation of the quantum Su-Schrieffer-Heeger model to in-plane classical lattice dynamics, illustrating the complex interactions between TEMs and NHSE.

2. Topological edge modes in Hermitian meta-lattices

We begin our study with the examination of a Hermitian local resonance-based meta-lattice featuring nontrivial topology, as depicted in Fig. 1(a) (Zhao et al., 2018). The unit cell of this meta-lattice comprises an inner mass m with displacement v_n^i and an outer mass M with displacement u_n^i , where i and n denote the intra-cellular position and unit cell index, respectively. The governing equations of motion for the meta-lattice are expressed as

$$\begin{aligned} -M\omega^2 u_n^1 &= k_2(u_{n-1}^2 - u_n^1) + k_1(u_n^2 - u_n^1) + k_m(v_n^1 - u_n^1), \\ -M\omega^2 u_n^2 &= k_1(u_n^1 - u_n^2) + k_2(u_{n+1}^1 - u_n^2) + k_m(v_n^2 - u_n^2), \\ -m\omega^2 v_n^1 &= k_m(u_n^1 - v_n^1), \\ -m\omega^2 v_n^2 &= k_m(u_n^2 - v_n^2), \end{aligned} \quad (1)$$

where k_1 and k_2 represent the intra- and inter-cellular Hookean springs, while k_m denotes the on-site Hookean spring connecting M and m . Considering PBCs, we define a set of harmonic displacements as $[u_n^1, u_n^2, v_n^1, v_n^2]^T = [u^1, u^2, v^1, v^2]^T e^{iqn}$, where $i = \sqrt{-1}$.

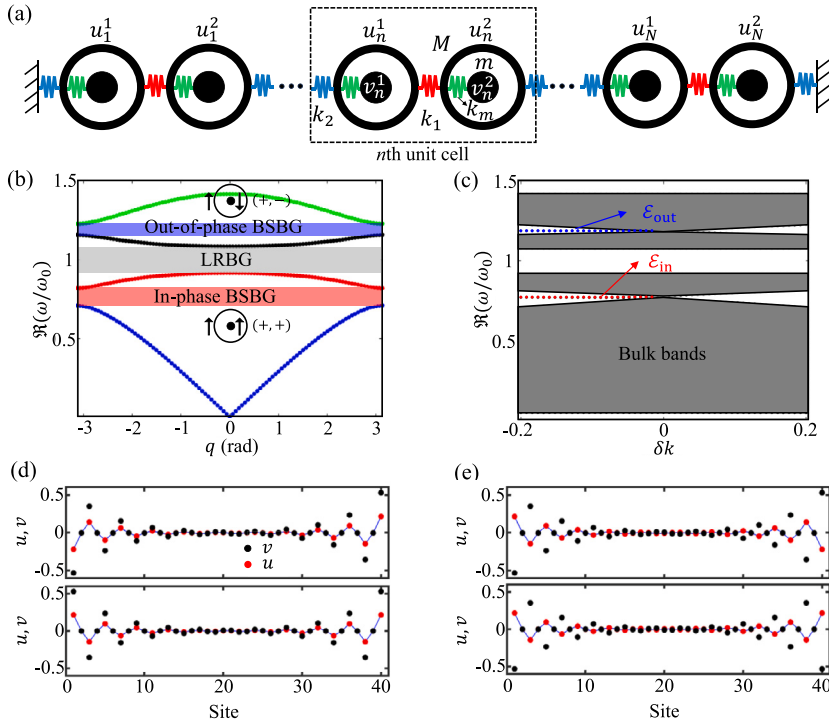


Fig. 1. (a) Schematics of the 1D Hermitian local resonance-based topological meta-lattice. (b) Band structure for $\delta k = -0.2$, with two highlighted BSBGs characterized by in-phase and out-of-phase motions between m and M . Between them is the LRBG centered at $\omega = \omega_0$. (c) δk -dependent bulk spectrum of a finite Hermitian meta-lattice consisting of 20 unit cells. Here, $M = 6m$ and $k_m = (k_1 + k_2)/5$ throughout the paper, and the TEMs (\mathcal{E}_{in} and \mathcal{E}_{out}) are highlighted. (d) Modal profiles of \mathcal{E}_{in} . (e) Modal profiles of \mathcal{E}_{out} . In both (d) and (e), the red and black points correspond to the outer masses M and inner masses m , respectively.

Therefore, Eq. (1) can be expressed in matrix form as

$$\omega^2 \underbrace{\begin{bmatrix} M & 0 & 0 & 0 \\ 0 & M & 0 & 0 \\ 0 & 0 & m & 0 \\ 0 & 0 & 0 & m \end{bmatrix}}_{\mathbf{M}} \mathbf{u} = \begin{bmatrix} k_t & -k_1 - k_2 e^{-iq} & -k_m & 0 \\ -k_1 - k_2 e^{iq} & k_t & 0 & -k_m \\ -k_m & 0 & k_m & 0 \\ 0 & -k_m & 0 & k_m \end{bmatrix} \mathbf{u}, \quad (2)$$

in which $k_t = k_1 + k_2 + k_m$, and $\mathbf{u} = [u^1, u^2, v^1, v^2]^T$. Eq. (2) can be further reduced into

$$\omega^2 M_{\text{eff}} \begin{bmatrix} u^1 \\ u^2 \end{bmatrix} = \begin{bmatrix} k_1 + k_2 & -k_1 - k_2 e^{-iq} \\ -k_1 - k_2 e^{iq} & k_1 + k_2 \end{bmatrix} \begin{bmatrix} u^1 \\ u^2 \end{bmatrix}, \quad (3)$$

in the presence of an effective mass density $M_{\text{eff}}(\omega) = M + \frac{m\omega_0^2}{\omega_0^2 - \omega^2}$, where the resonance frequency reads $\omega_0^2 = k_m/m$. Using Eq. (3), we can derive the band structure of the Hermitian meta-lattice with $\delta k \equiv (k_1 - k_2)/(k_1 + k_2) = -0.2$, as shown in Fig. 1(b). In this context, while the first and third band gaps represent BSBGs arising from inter-cellular wave scattering, the second band gap is a local resonant band gap (LRBG) resulting from the local resonance of each individual on-site scattering unit (Liu et al., 2000). Notably, the LRBG persists even when $\delta k = 0$, a scenario in which the two BSBGs are closed.

Next, we delve into the topological characteristics of the Hermitian meta-lattice with $\delta k \neq 0$. By subtracting $(k_1 + k_2)\mathbb{I}$ from both sides of Eq. (3), we arrive at the eigenvalue problem of a conventional Su-Schrieffer-Heeger chain, expressed as

$$\lambda \begin{bmatrix} u^1 \\ u^2 \end{bmatrix} = \begin{bmatrix} 0 & k_1 + k_2 e^{-iq} \\ k_1 + k_2 e^{iq} & 0 \end{bmatrix} \begin{bmatrix} u^1 \\ u^2 \end{bmatrix}, \quad (4)$$

where $\lambda = k_1 + k_2 - M_{\text{eff}}\omega^2$. The dynamic matrix exhibits chiral symmetry, ensuring that the resulting eigenvalues occur in pairs, i.e., $\pm \lambda$. The Su-Schrieffer-Heeger chain demonstrates nontrivial bulk topology, characterized by a nonzero winding number when $\delta k < 0$, and is topologically trivial when $\delta k > 0$. The nontrivial topology can also be confirmed by calculating the Zak phase for each band, as described by Eq. (2) (Zhao et al., 2018). This nontrivial bulk topology indicates the presence of in-gap TEMs for $\delta k < 0$ within a finite Su-Schrieffer-Heeger chain under OBCs, as depicted in Fig. 1(c).

Additionally, the modal profiles of the TEMs can be obtained analytically. The OBCs schematically shown in Fig. 1(a) can be described by eliminating $v_n^{1,2}$ as

$$\begin{aligned}-M_{\text{eff}}\omega^2 u_1^1 &= -(k_1 + k_2)u_1^1 + k_1 u_1^2, \\ -M_{\text{eff}}\omega^2 u_N^2 &= -(k_1 + k_2)u_N^2 + k_2 u_N^1.\end{aligned}\quad (5)$$

For the TEMs of a finite Su–Schrieffer–Heeger chain with eigenvalue denoted as $\lambda_{\text{TEM}} = k_1 + k_2 - M_{\text{eff}}\omega_{\text{TEM}}^2 = 0$, we have

$$\begin{aligned}k_2 u_n^2 + k_1 u_{n+1}^2 &= 0; \quad k_1 u_1^2 = 0, \\ k_1 u_n^1 + k_2 u_{n+1}^1 &= 0; \quad k_2 u_N^1 = 0.\end{aligned}\quad (6)$$

For a finite N , the above equations do not yield solutions, but as N tends towards infinity, they give rise to left- and right-localized TEMs (Asbóth et al., 2016). The modal profile of the left-localized TEM is expressed as

$$u_n^{1L} = \left(-\frac{k_2}{k_1}\right)^{-n}, \quad u_n^{2L} = 0, \quad (7)$$

whereas that of the right-localized TEM is expressed as

$$u_n^{1R} = 0, \quad u_n^{2R} = \left(-\frac{k_2}{k_1}\right)^n. \quad (8)$$

The modal profiles of the inner masses m for the left- and right-localized TEMs can be determined by substituting Eqs. (7) and (8) into the last two harmonic equations of Eq. (1). These profiles are expressed as

$$v_n^{1L} = \frac{\omega_0^2}{\omega_0^2 - \omega_{\text{TEM}}^2} \left(-\frac{k_2}{k_1}\right)^{-n}, \quad v_n^{2L} = 0, \quad (9)$$

and

$$v_n^{1R} = 0, \quad v_n^{2R} = \frac{\omega_0^2}{\omega_0^2 - \omega_{\text{TEM}}^2} \left(-\frac{k_2}{k_1}\right)^n. \quad (10)$$

There are two solutions for eigenfrequencies ω_{TEM} . The smaller one $\omega_{\text{TEM}} \equiv \omega_{\text{in}}$, satisfying $\omega_0^2/(\omega_0^2 - \omega_{\text{TEM}}^2) > 0$, corresponds to the in-phase TEM, labeled as \mathcal{E}_{in} , which exhibits in-phase motion between m and M (see Fig. 1(d)). For the greater one $\omega_{\text{TEM}} \equiv \omega_{\text{out}}$, satisfying $\omega_0^2/(\omega_0^2 - \omega_{\text{TEM}}^2) < 0$, the corresponding TEM, labeled as \mathcal{E}_{out} , features out-of-phase motion between m and M (see Fig. 1(e)).

For a finite N chain, both the modal profiles of \mathcal{E}_{in} and \mathcal{E}_{out} are linear combinations of their modal profiles with infinite N , as given in Eqs. (7) and (8), with coefficients $(1, 1)$ and $(1, -1)$, respectively, according to degenerate perturbation theory (Asbóth et al., 2016). Therefore, within the finite Su–Schrieffer–Heeger chain, both \mathcal{E}_{in} and \mathcal{E}_{out} exhibit in-phase and out-of-phase localized profiles at the ends of the lattice, as illustrated in Fig. 1(d) and (e).

3. Non-Hermitian skin effect in non-Hermitian meta-lattices

This section focuses on the NHSE in a non-Hermitian locally resonant meta-lattice in the context of classical mechanics. As has been mentioned in the introduction, NHSE refers to a phenomenon where bulk modes of a finite system behave as skin modes collapsing to the open boundaries, with their quantity scaling with the volume of the system. To access the NHSE, the non-Hermitian meta-lattice is designed with a feedback sensing-actuating loop controlled by a programmable transfer function H , as depicted in Fig. 2(a). Such a discrete active system can be physically realized by a continuous beam system featured with feedback control loops, as discussed in Appendix A. An active control loop, comprising a strain sensor, an actuator, and the transfer function H , is capable of detecting the stretching of the spring k_m on the second site of the n th unit cell and applying an actuation force to the outer mass M on the first site of the $(n+1)$ th unit cell. Both the sensor and actuator can be implemented using piezoelectric materials, while the transfer function can be realized through a series of analog electronics or a digital controller (Wu et al., 2022; Chen et al., 2021b; Wu et al., 2023a); see also Fig. A.16(b) in Appendix A. Unlike Hermitian systems, a non-Hermitian system governed by a non-Hermitian dynamic matrix or Hamiltonian exhibits complex eigenvalues. The real part of these eigenvalues corresponds to energy storage, while the imaginary part corresponds to energy exchange with external agents.

By modifying Eq. (1), the governing equation of the non-Hermitian meta-lattice can be obtained as

$$\begin{aligned}-M\omega^2 u_n^1 &= k_2(u_{n-1}^2 - u_n^1) + k_1(u_n^2 - u_n^1) + k_m(v_n^1 - u_n^1) + H(v_{n-1}^2 - u_{n-1}^2), \\ -M\omega^2 u_n^2 &= k_1(u_n^1 - u_n^2) + k_2(u_{n+1}^1 - u_n^2) + k_m(v_n^2 - u_n^2), \\ -m\omega^2 v_n^1 &= k_m(u_n^1 - v_n^1), \\ -m\omega^2 v_n^2 &= k_m(u_n^2 - v_n^2).\end{aligned}\quad (11)$$

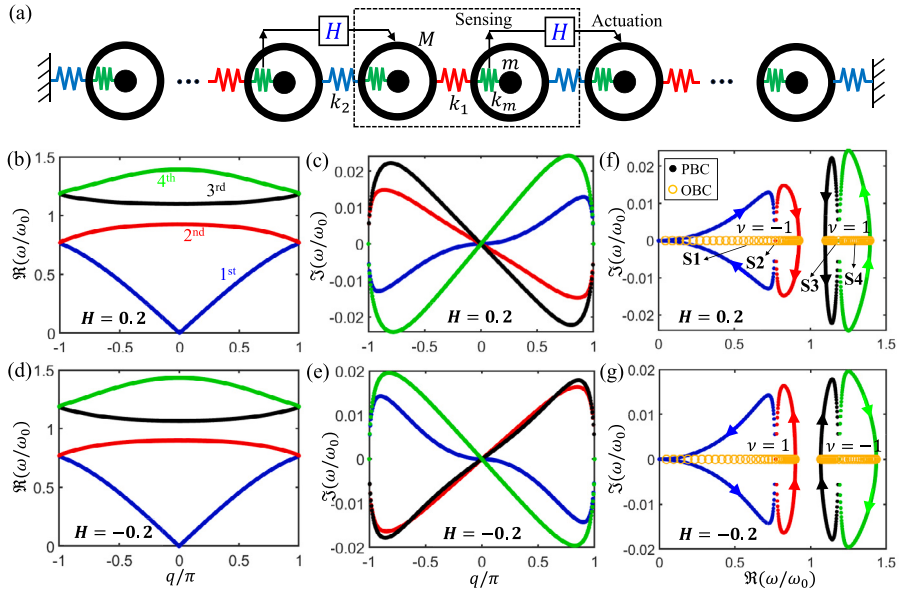


Fig. 2. Non-Hermitian meta-lattice enables opposite field localization directions among the two BSBGs. (a) Schematics of the non-Hermitian meta-lattice subjected to a feedback control modulation with a transfer function H . (b,c) Real and imaginary dispersion curves with $H = 0.2$ and $\delta k = 0$ under PBCs. (d,e) Real and imaginary dispersion curves with $H = -0.2$ and $\delta k = 0$ under PBCs. (f,g) Comparison of the PBC (solid points) and the corresponding OBC (circles) spectra. Four representative modes (S1–S4) are selected above and below the LRBG. Among them, modes S1 and S4 are located at $\omega/\omega_0 = 0.5623$ and 1.2615, respectively, whereas modes S2 and S3 are located at the kissing nodes of adjacent loops, i.e., $\omega/\omega_0 = 0.7693$ and 1.1189. Each loop is characterized by the winding number v calculated using Eq. (14). The arrows indicate the evolution or winding directions as q is swept from $-\pi$ to π .

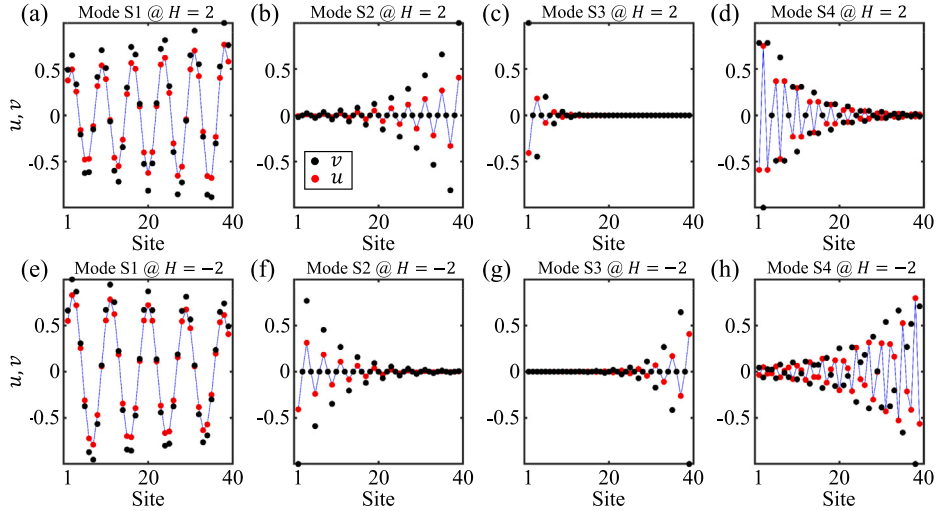


Fig. 3. Demonstrations of non-Hermitian skin modes within a homogeneous ($\delta k = 0$) non-Hermitian meta-lattice consisting of 20 unit cells. (a-d) Spatial profiles of selected skin modes S1–S4 in Fig. 2(f) for $H = 0.2$. (e-h) Spatial profiles of selected skin modes S1–S4 in Fig. 2(g) for $H = -0.2$. The selected modes correspond to $\omega/\omega_0 = 0.5623, 0.7693, 1.1189$, and 1.2615.

Under PBCs, Eq. (11) can be rewritten into

$$\omega^2 \mathbf{M} \mathbf{u} = \underbrace{\begin{bmatrix} k_t & -k_1 - (k_2 - H)e^{-iq} & -k_m & -He^{-iq} \\ -k_1 - k_2 e^{iq} & k_t & 0 & -k_m \\ -k_m & 0 & k_m & 0 \\ 0 & -k_m & 0 & k_m \end{bmatrix}}_{\mathbf{D}} \mathbf{u}. \quad (12)$$

By eliminating the terms $v^{1,2}$, the equations of motion can be further reduced into

$$\omega^2 \begin{bmatrix} M_{\text{eff}} & M_{\text{odd}} \\ 0 & M_{\text{eff}} \end{bmatrix} \begin{bmatrix} u^1 \\ u^2 \end{bmatrix} = \begin{bmatrix} k_1 + k_2 & -k_1 - k_2 e^{-iq} \\ -k_1 - k_2 e^{iq} & k_1 + k_2 \end{bmatrix} \begin{bmatrix} u^1 \\ u^2 \end{bmatrix}, \quad (13)$$

where an effective odd mass $M_{\text{odd}} = \frac{H}{\omega_0^2 - \omega^2} e^{-iq}$ emerges as a nonzero off-diagonal term, representing an unbalanced force between the two outer masses (Wu et al., 2023a). The non-Hermiticity of the system arises from this odd mass term controlled by H . Complex dispersion diagrams for the non-Hermitian lattice are plotted in Fig. 2(b–e) for $H = 0.2$ and $H = -0.2$, with $\delta k = 0$ (i.e., $k_1 = k_2$) which eliminates topological characteristics. Non-Hermitian systems with nonzero nonreciprocal interactions, such as H in this work, do not adhere to conventional energy conservation. Consequently, nonzero imaginary components $\Im(\omega/\omega_0)$ emerge for all four wave bands (see Fig. 2(c) and (e)), and their amplitudes and signs, along with the real components $\Re(\omega/\omega_0)$, are controlled by H ; see Fig. B.17 in Appendix B. Nonzero $\Im(\omega/\omega_0)$ typically indicates energetic amplification or attenuation for waves propagating along specific directions. This energetic exchange can be understood by calculating the total work done by the feedback control H per cycle at a finite frequency (Chen et al., 2021b; Scheibner et al., 2020; Wu et al., 2023a); refer to Appendix B for more details. When H performs positive/negative work, propagating waves are amplified/attenuated, leading to negative/positive $\Im(\omega/\omega_0)$, as illustrated in Fig. B.18(a) and (b).

We now investigate how non-Hermiticity affects the topological properties of bulk modes in a finite homogeneous ($\delta k = 0$) non-Hermitian meta-lattice, specifically in the context of NHSE. To demonstrate the skin bulk modes induced by NHSE, we begin by calculating the OBC spectra for a finite non-Hermitian meta-lattice consisting, composed of 40 unit cells and terminated with fixed boundary conditions at both ends, as shown in Fig. 2(a). The corresponding complex PBC spectra are obtained from Fig. 2(b–e) by sweeping q from $-\pi$ to π . In Fig. 2(f) and (g), the complex PBC and OBC spectra are plotted as functions of $\Re(\omega/\omega_0)$ and $\Im(\omega/\omega_0)$ for $H = 0.2$ and $H = -0.2$, respectively. The OBC spectra are noticeably different from the PBC ones. Specifically, bulk modes of a finite non-Hermitian meta-lattice, which are spectrally encircled by complex PBC bands, exhibit NHSE and consequently display modal profiles exponentially localized to one end of the finite meta-lattice. To predict the localization directions, one can directly calculate the winding number $v(\omega)$ based on the complex PBC spectra given in Fig. 2(f) and (g) as

$$v(\omega) = \int_0^{2\pi} \frac{dq}{2\pi i} \frac{d}{dq} \log[\omega_a(q) - \omega], \quad (14)$$

in which $\omega_a(q)$ denotes the frequency of band a at wave number q , and ω represents a reference frequency. The winding number $v(\omega)$ indicates whether a system hosts a localized bulk mode (or skin mode) at ω (Gong et al., 2018; Okuma et al., 2020; Zhang et al., 2020; Chen et al., 2021b; Wang et al., 2024). As depicted in Fig. 2(f), when $H > 0$, the lower two bands wind clockwise with $v = -1$ from $q = -\pi$ to $q = \pi$. Bulk modes supported by the corresponding non-Hermitian meta-lattice and encircled by these two complex bands are right-localized skin modes; see Fig. 3(a) and (b). Conversely, the upper two bands wind counterclockwise, corresponding to $v = 1$. Bulk modes encircled by these two complex bands are left-localized skin modes; see also Fig. 3(c) and (d). For $H < 0$, the localization directions are reversed (Fig. 3(e–h)), because the winding directions of all complex bands are reversed, as shown in Fig. 2(g). Additionally, the degrees of localization of skin modes depend on their eigenfrequencies. To interpret this, we can calculate the inverse penetration depth represented by $\Im(q)$ for ω (Chen et al., 2021b). This involves considering a complex $q = \Re(q) + i\Im(q)$ and a real ω while solving the eigenvalue problem stated in Eq. (13). While $\Re(q)$ constructs the real-valued band structure given in Fig. 2(b) and (d), $\Im(q)$ indicates that the associated wave modes are spatially asymmetric, either amplified or attenuated exponentially towards one end. In the scenarios presented in Fig. 3, the larger $|\Im(q)|$ is, the stronger the field localization of a skin mode towards a certain end will be. A detailed study is presented in Appendix B.

4. Topological edge modes in the non-Hermitian meta-lattice

In non-Hermitian systems, localized edge modes encompass both skin modes and TEMs. While both are localized at the system's edges, skin modes – similar to bulk modes in Hermitian systems – are susceptible to disorder. In contrast, TEMs exhibit robustness against perturbations. The emergence of TEMs is predictable through the bulk topological invariant, adhering to the principle of bulk-edge correspondence. However, the conventional bulk-edge correspondence, which relies on Bloch band theory in Hermitian systems, does not apply to non-Hermitian systems (Yao and Wang, 2018; Bergholtz et al., 2021; Yokomizo and Murakami, 2019; Kunst et al., 2018). To re-establish the bulk-edge correspondence in this work, it is necessary to generalize the wavenumber q from real to complex values, thereby extending Bloch band theory into non-Bloch band theory. We will numerically validate the bulk-edge correspondence using the framework of non-Bloch band theory.

We begin by considering an inhomogeneous non-Hermitian meta-lattice with lattice dimerization $\delta k \neq 0$, depicted in Fig. 2(a) and characterized by Eq. (11). Similar to the previously discussed non-Hermitian meta-lattice with $\delta k = 0$, the presence of H breaks the Hermiticity of the lattice system. However, unlike the Hermitian meta-lattice or conventional Su-Schrieffer-Heeger chain presented in Fig. 1, chiral symmetry does not apply to the current non-Hermitian meta-lattice. Here, we attempt to examine the topological property of the non-Hermitian meta-lattice by directly calculating the Zak phase θ_a , which is a 1D bulk topological invariant (Mehri-Dehnavi and Mostafazadeh, 2008; Zhang et al., 2019; He and Chien, 2020; Chiu et al., 2016). When $\theta_a/2\pi$ is quantized by half-integer values, the associated band exhibits nontrivial bulk topology, leading to the emergence of in-gap TEMs within finite lattices with OBCs. This is the consequence of the bulk-edge correspondence. However, in our scenario, the explicit

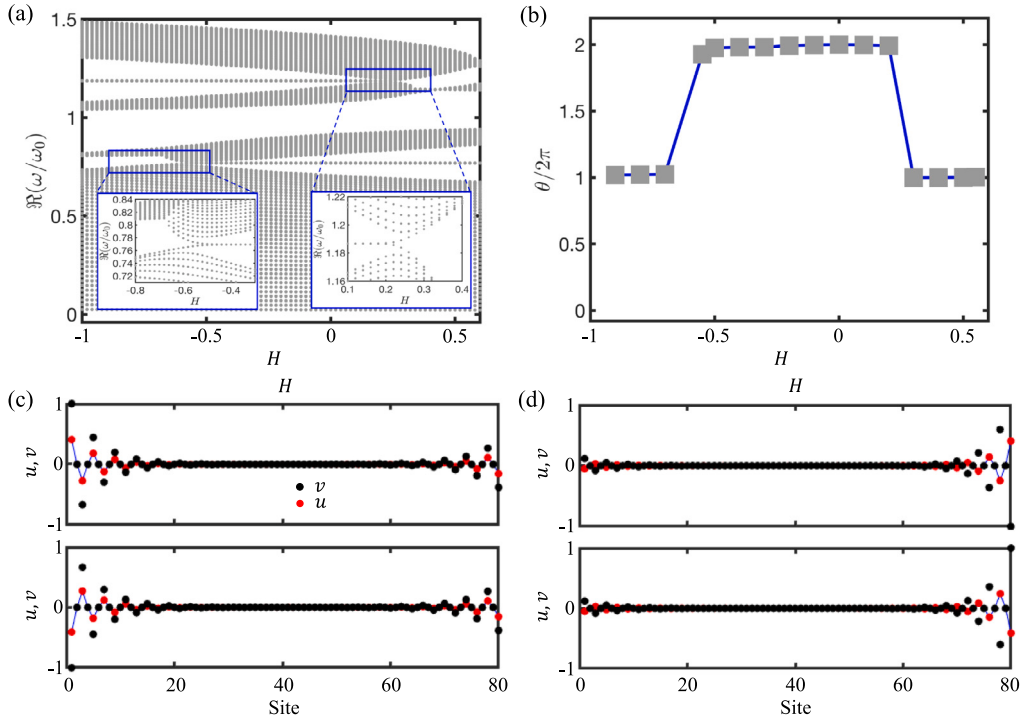


Fig. 4. Numerical computation of the topological invariant for the non-Hermitian meta-lattice with $\delta k = -0.2$. (a) OBC spectrum of an open even-site non-Hermitian meta-lattice with 40 unit cells. The insets display the magnified views of the bifurcation areas. (b) Sum of Zak phases of all bands as a function of H . (c) Modal profiles of E_{in} at $H = -0.05$. (d) Modal profiles of E_{out} at $H = -0.05$. In both (c) and (d), the red and black points correspond to displacements of the outer masses M and inner masses m , respectively.

symmetry is not apparent. Therefore, to ascertain the nontrivial nature of the bulk topology in our system, we calculate the Zak phase directly for the α th ($\alpha = 1, 2, 3$, and 4) band as

$$\theta_\alpha = i \int_{C_{\beta_\alpha}} \mathbf{u}_\alpha^L \frac{d\mathbf{u}_\alpha^R}{d\beta} d\beta, \quad (15)$$

in which \mathbf{u}_α^L and \mathbf{u}_α^R are the left and right normalized eigenvectors for the α th eigenmode. They are obtained from the following two eigenvalue problems

$$\begin{aligned} \mathbf{D}(\beta)\mathbf{u}_\alpha^R &= \Omega_\alpha \mathbf{M}\mathbf{u}_\alpha^R, \\ \mathbf{D}^\dagger(\beta)\mathbf{u}_\alpha^L &= \Omega_\alpha^*\mathbf{M}^\dagger\mathbf{u}_\alpha^L, \end{aligned} \quad (16)$$

with $\beta = e^{iq}$, \dagger and $*$ denote the Hermitian transpose and complex conjugate operations, respectively. The first equation in Eq. (16) is the same as Eq. (12), but we denote \mathbf{u} as \mathbf{u}_α^R and ω^2 as Ω_α . In a non-Hermitian system, $\mathbf{D}^\dagger \neq \mathbf{D}$ and $\mathbf{M}^\dagger \neq \mathbf{M}$, so the eigenvalues and eigenvectors of \mathbf{D}^\dagger and \mathbf{M}^\dagger are different from those in Eq. (12), and the eigenvectors of Eq. (12) are not orthogonal. We define the eigenvalue problem of \mathbf{D}^\dagger and \mathbf{M}^\dagger in the second equation in Eq. (16). The eigenvectors \mathbf{u}_α^L and \mathbf{u}_α^R have a biorthogonal relation, which is an extension of the conventional orthogonal relation in Hermitian systems (Ashida et al., 2020). C_{β_α} represents the generalized Brillouin zone (GBZ) for the band $\alpha = 1, 2, 3, 4$, which extends the traditional notion of the Brillouin zone from Hermitian to non-Hermitian systems. In a Hermitian system, the GBZ is a unit circle in the complex plane. However, it is generally extended into an irregular loop in the complex plane and varies among each dispersion band (Yao and Wang, 2018; Yokomizo and Murakami, 2019). For our system, the GBZ does not have general analytical expressions, but can be determined numerically by solving the following two algebraic equations

$$\begin{aligned} \det[\mathbf{D}(\beta) - \Omega\mathbf{M}] &= 0, \\ |\beta_2(\Omega)| &= |\beta_3(\Omega)|, \end{aligned} \quad (17)$$

where β_2 and β_3 represent the second and third largest roots, ranked by magnitude, of the first equation in Eq. (17). Finally, the Zak phase can be calculated by numerically integrating Eq. (15), where the derivative of the right eigenvector is approximated using the finite difference method. Fig. 4(a) presents the calculated OBC spectra for a 40-unit-cell non-Hermitian meta-lattice under OBCs, while Fig. 4(b) shows the total Zak phase $\theta = \sum_{\alpha=1}^4 \theta_\alpha$, calculated from Eq. (15). For $H \in (-1, -0.6)$, θ is always 2π . This predicts the existence of TEMs within one of the BSBGs; see Fig. 4(a). At $H \approx -0.6$, θ jumps from 2π to 4π at $H \approx -0.6$, which corresponds

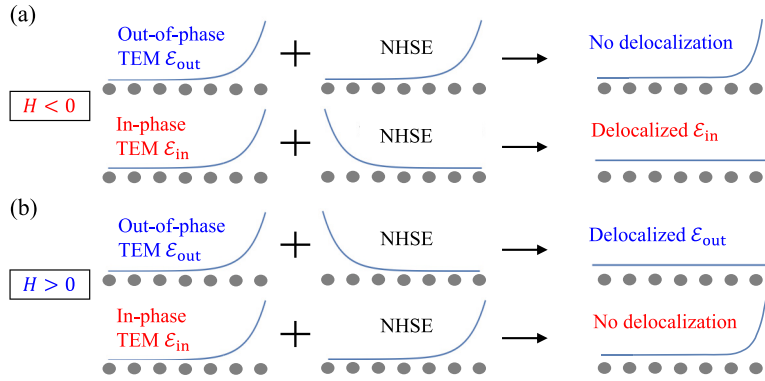


Fig. 5. Schematic illustration of the asymmetric TEM delocalization, where the counterbalancing of NHSE can exclusively delocalize either (a) ϵ_{in} or (b) ϵ_{out} , depending on the sign of H . The TEM, which is not delocalized, retains a stronger localized presence on the right edge.

to the bifurcation point of the two TEMs calculated with OBCs within the in-phase BSBG (Fig. 4(a)). For $H \in (-0.6, 0.3)$, θ is 4π which indicates the existence of TEMs within both BSBGs. At $H \approx 0.3$, θ jumps from 4π to 2π at $H \approx 0.3$, which corresponds to the bifurcation point of the two TEMs calculated with OBCs within the out-of-phase BSBGs. For $H \in (0.3, 0.6)$, θ is 2π which indicates the existence of TEMs within one BSBG. In Fig. 4(c) and (d), we present the modal profiles of ϵ_{in} and ϵ_{out} , respectively, at $H = -0.05$. Compared with modal profiles at $H = 0$ given in Fig. 1(d) and (e), the left field localization of ϵ_{in} is enhanced whereas the right field localization is suppressed (Fig. 4(c)). On the contrary, the change in left and right field localization for ϵ_{out} is opposite (Fig. 4(d)). This is due to the opposite field localization of NHSE, as previously shown in Fig. 3(e-h) for $H < 0$.

5. Delocalization of topological edge modes in the non-Hermitian meta-lattice

The essence of this work is the exploration of the asymmetric delocalization of TEMs within the framework of classical mechanics, as schematically illustrated in Fig. 5. In addition to the nonreciprocal coupling by the feedback control, the dynamics brought about by the local resonance can also significantly modify the competition between NHSE and TEMs, mainly due to the opposing forces at work within the upper and lower BSBGs (see Figs. 2 and 3). It is evident that the emerging asymmetry is fundamentally tied to the opposite localization tendencies of NHSE within the upper and lower bands, a unique outcome of our particular feedback connection strategy. In what follows, we will delve deeper into this intriguing phenomenon by conducting rigorous analytical investigations.

In Section 3, it is found that the TEMs of the finite chain are localized at both ends. To achieve TEMs localized at the one end, a straightforward approach is to remove a lattice site at the opposite end to disrupt the chiral symmetry. As a result, the TEM is only localized at the one end. As shown in Fig. 6(a), for a Hermitian meta-lattice ($H = 0$) with the leftmost site (u_1^1 and v_1^1) removed, the boundary conditions are given by

$$\begin{aligned} -M_{\text{eff}}\omega^2 u_1^2 &= -(k_1 + k_2)u_1^2 + k_2u_2^1, \\ -M_{\text{eff}}\omega^2 u_N^2 &= -(k_1 + k_2)u_N^2 + k_1u_N^1. \end{aligned} \quad (18)$$

Substituting $\lambda_{\text{TEM}} = 0$ into (18), we have

$$\begin{aligned} k_1u_n^1 + k_2u_{n+1}^1 &= 0, \quad k_1u_N^1 = 0, \\ k_2u_n^2 + k_1u_{n+1}^2 &= 0, \quad k_2u_2^1 = 0. \end{aligned} \quad (19)$$

In the absence of the left-localized TEMs, the modal profiles of the right-localized TEMs within the Hermitian meta-lattice are described by

$$u_n^{1R} = 0, \quad u_n^{2R} = \left(-\frac{k_2}{k_1}\right)^n, \quad v_n^{1R} = 0, \quad v_n^{2R} = \frac{\omega_0^2}{\omega_0^2 - \omega_{\text{TEM}}^2} \left(-\frac{k_2}{k_1}\right)^n, \quad (20)$$

Next, we activate the feedback control, transforming the Hermitian meta-lattice into a non-Hermitian one with $H \neq 0$. The eigenfrequencies of TEMs in the non-Hermitian meta-lattice are always ω_{TEM} , regardless of the value of H , as proved in Appendix C. Based on this, we examine the modal profiles of the right-localized TEMs. Eq. (C.5) can be reduced to the equations of motion for only outer masses M by eliminating the inner mass degree of freedom, reading

$$\begin{aligned} k_1u_n^1 + k_2u_{n+1}^1 &= 0, \quad k_1u_N^1 = 0, \\ k_2u_n^2 + k_1u_{n+1}^2 + \lambda_{\text{odd}}u_n^2 &= 0, \quad k_2u_2^1 = 0, \end{aligned} \quad (21)$$

where

$$\lambda_{\text{odd}} = \frac{\omega_{\text{TEM}}^2 H}{\omega_0^2 - \omega_{\text{TEM}}^2}. \quad (22)$$

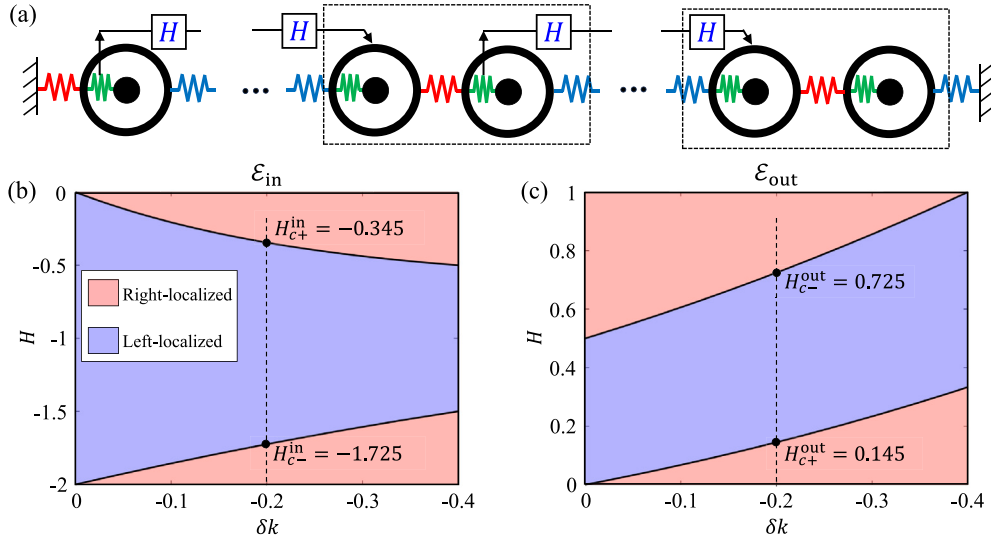


Fig. 6. Phase diagrams of the TEMs as functions of H and δk . (a) Schematic illustration of the non-Hermitian meta-lattice including 15 unit cells with the leftmost site removed. The dashed boxes indicate the complete unit cells. (b,c) Phase diagrams indicating the localization directions of (b) \mathcal{E}_{in} and (c) \mathcal{E}_{out} . The red and blue hatches correspond to right and left localization. The black solid curves correspond to the phase transitions or critical transfer functions $H_{c\pm}^{\text{in,out}}$ where TEM delocalization occurs. The dashed lines indicate $\delta k = -0.2$, which is considered in the following. The corresponding critical transfer functions are highlighted.

The solutions for the right-localized TEMs in the non-Hermitian meta-lattice are

$$\begin{aligned} u_n^{1R} &= 0, \quad u_n^{2R} = \left(-\frac{k_2 + \lambda_{\text{odd}}}{k_1} \right)^n, \\ v_n^{1R} &= 0, \quad v_n^{2R} = \frac{\omega_0^2}{\omega_0^2 - \omega_{\text{TEM}}^2} \left(-\frac{k_2 + \lambda_{\text{odd}}}{k_1} \right)^n. \end{aligned} \quad (23)$$

It can be observed from Eq. (23) that H affects the modal profile of the right-localized TEMs without altering the corresponding eigenfrequencies. Moreover, compared with the modal profile of the Hermitian TEM described in Eq. (20), the non-Hermitian case differs in only one aspect: k_2 is replaced with $k_2 + \lambda_{\text{odd}}$. While $k_2 + \lambda_{\text{odd}}$ specifically applies to the TEMs, it does not affect the description of other bulk modes. As a special case, We consider

$$\left| \frac{k_2 + \lambda_{\text{odd}}}{k_1} \right| = 1, \quad (24)$$

indicating that u_n^{2R} and v_n^{2R} exhibit constant magnitude across the entire non-Hermitian meta-lattice. Therefore, the right-localized TEMs are extended and delocalized. To Eq. (24), there are two solutions for H , which read

$$H_{c\pm}^{\text{in,out}} = \frac{(-k_2 \pm k_1)(\omega_0^2 - \omega_{\text{TEM}}^2)}{\omega_{\text{TEM}}^2}. \quad (25)$$

where H_{c+} (H_{c-}) is the critical transfer function that causes TEM delocalization with in-phase (out-of-phase) motion between u_n^{2R} and u_{n+1}^{2R} within the lower (upper) BSBG. Based on Eq. (25), we plot in Fig. 6 the phase diagrams for both \mathcal{E}_{in} and \mathcal{E}_{out} for the non-Hermitian meta-lattice with $\delta k < 0$ shown in Fig. 6(a). Starting from $H = 0$, the meta-lattice is Hermitian and only features right-localized TEMs. As $|H|$ increases, both \mathcal{E}_{in} and \mathcal{E}_{out} experience phase transitions at differently valued H_c^\pm with significantly distinct transition behaviors, due to the difference between ω_{in} and ω_{out} . For clear observation, the complex OBC spectra for the non-Hermitian meta-lattice presented in Fig. 6(a) are illustrated in Fig. 7(a) and (b), respectively, with $\delta k = -0.2$ and $H \in [-2, 2]$. Several observations can be made. First, when $H > 0$ ($H < 0$), \mathcal{E}_{in} (\mathcal{E}_{out}) is always gapped from the bulk, indicating no delocalization occurs. Second, when $H > 0$, \mathcal{E}_{out} undergoes multiple phase transitions. We take \mathcal{E}_{out} as an example due to its similarity with \mathcal{E}_{in} . As can be seen from Fig. 7(c), the out-of-phase BSBG goes through an open-closed-reopen-reclosed process. The transition points $H_{c\pm}^{\text{out}}$ determined from Eq. (24) reveal that \mathcal{E}_{out} should be delocalized by the NHSE twice as H increases owing to the quadratic form of λ_{odd} given in Eq. (22). In order to showcase this intriguing behavior, we highlight five representative modes I–V for $H > 0$, together with the Hermitian ($H = 0$) mode \mathcal{H} .

The PBC and OBC spectra and the spatial profiles of the two TEMs around the first phase transitions $H_{c+}^{\text{in,out}}$ are plotted in Fig. 8. As can be seen from Fig. 8(a), at mode I ($H = 0.1$), the upper two bands form isolated loops on the complex PBC domain, and \mathcal{E}_{out} is gapped, which is detailed in Fig. 8(d) for mode I, meaning that the localization direction of mode I is identical to that of mode \mathcal{H} . At mode II with the critical $H_{c+}^{\text{out}} = 0.145$, ω_{out} falls exactly on the right edge ($q = \pi$) of the PBC loop of the third band;

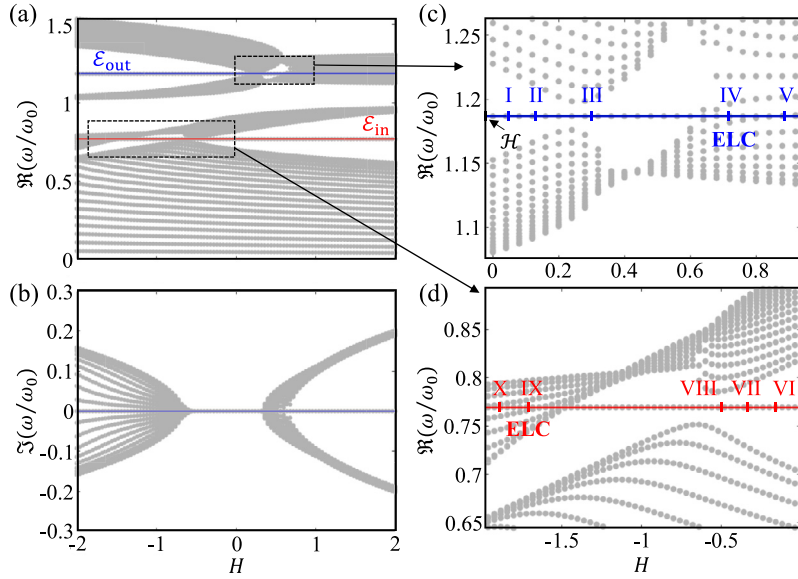


Fig. 7. Robustness of the TEMs against random disorders when $H \neq 0$. (a,b) The complex bulk spectra for the non-Hermitian meta-lattice depicted in Fig. 6(a) are shown as a function of H , with $\delta k = -0.2$. The two TEMs are highlighted by the blue and red lines. (c,d) Magnified views of the bulk spectra around the phase transitions for (c) ϵ_{out} and (d) ϵ_{in} . Ten representative modes are selected at different H . Specifically, the transfer functions for all the representative modes are selected to be $H_{IIIc} = 0$, $H_I = 0.1$, $H_{II} = 0.145$, $H_{III} = 0.3$, $H_{IV} = 0.725$, $H_V = 0.9$, $H_{VI} = -0.1$, $H_{VII} = -0.345$, $H_{VIII} = -0.5$, $H_{IX} = -1.725$, and $H_X = -1.9$.

see detailed spectrum for mode II in Fig. 8(d). This implies that ϵ_{out} is perfectly delocalized (Fig. 8(c) for mode II), exhibiting $u_n^{1,2} = -u_{n+1}^{1,2}$ and $v_n^{1,2} = -v_{n+1}^{1,2}$. The delocalization of ϵ_{out} takes place when the field localization of ϵ_{out} and that of the NHSE are opposite, balanced, and cancel each other. Keeping increasing H to reach mode III ($H = 0.3$), the out-of-phase BSBG vanishes, and the third and fourth bands forms a new loop on the complex PBC domain. ϵ_{out} is now encircled by this loop, and its spatial profile is relocalized to the left (Fig. 8(c) for mode III). The relocalization takes place due to the NHSE overpowering the TEM in terms of localization strength. On the other hand, during the delocalization process of ϵ_{out} , the field localization directions of the NHSE and ϵ_{in} are always identical. As a result, the field localization of ϵ_{in} is enhanced by the NHSE (Fig. 8(b) for modes I, II, and III). This asymmetric delocalization between ϵ_{in} and ϵ_{out} results from the opposite localization of NHSE illustrated in Fig. 3(a-d), where it is shown that when $H > 0$, the NHSE causes right and left field localization for the lower and upper two bands, respectively. Continuing increasing H to mode IV to reach another critical $H_{c+}^{out} = 0.725$ and further going beyond H_{c+}^{out} , ϵ_{out} becomes delocalized again and eventually relocalize back to the right (see Fig. C.19(a) and (b) in Appendix D). Similar to ϵ_{out} , ϵ_{in} exhibits the same phase transition behavior accompanied with an open-closed-reopen-reclosed process for the in-phase BSBG as $H < 0$ decreases. The two critical transfer functions $H_{c\pm}^{in}$ causing phase transitions and delocalization of ϵ_{in} are obtained to be $H_{c+}^{in} = -0.345$ and $H_{c-}^{in} = -1.725$ from Eq. (24). Accordingly, $H_{c+}^{in} = -0.345$ features a modal profile of $u_n^{1,2} = -u_{n+1}^{1,2}$ and $v_n^{1,2} = -v_{n+1}^{1,2}$, since ω_{in} falls exactly on the left edge of the second PBC loop ($q = \pi$); see mode VII in Fig. 8(d). During the phase transition process of ϵ_{in} , ϵ_{out} remains localized to the right with enhanced localization strength. Again, This difference arises because for $H < 0$, the NHSE induced by the feedback control causes left and right field localization, respectively, for the lower two bands and the upper two bands; see Fig. 3(e-h).

It is also interesting to examine the robustness of the TEMs, whether or not they are delocalized, against random disorders or perturbations in the system parameters of the non-Hermitian meta-lattice. Geometric imperfections and material damping, which are commonly encountered in fabrication and experiments, can exist in real structures (see Fig. A.16) and effectively introduce complex-valued perturbations into the corresponding discrete model. Furthermore, low-pass filters typically used in active wave control experiments result in a transfer function of the form $H(\omega) = H_0 / (\frac{\omega^2}{\omega_0^2} + i\frac{\eta\omega}{\omega_0} + 1)$, where ω_0 and η correspond to the cut-off frequency and damping coefficient, respectively (Wu et al., 2023a; Chen et al., 2021b). This means that the transfer function H in real experiments may not always be real-valued and can carry non-negligible imaginary components. To account for these practical considerations, we introduce real-valued perturbations into the system parameters M and m in the form of $X_{\text{perturbation}} = \Re(X)$, and complex-valued perturbations into $k_{1,2,m}$ and H in the form of $X_{\text{perturbation}} = \Re(X) + i\Im(X)$. Fig. 9 illustrates corresponding eigenmodes for four types of real-valued random disorders ranging from 15% to 25%. As shown, both ϵ_{in} and ϵ_{out} , whether exhibiting delocalized or enhanced localization, retain their modal profiles with minor perturbations, indicating the robustness of the system. Fig. 10 demonstrates the impact of imaginary perturbations on the modal profiles of ϵ_{in} and ϵ_{out} at their respective delocalization transfer functions H_{c+}^{in} and H_{c+}^{out} . As shown in Fig. 10(a-c) for the case of H_{c+}^{in} , the delocalized ϵ_{in} and ϵ_{out} with enhanced localization remain largely unaffected by these imaginary perturbations, despite some minor local perturbations on the modal profiles. As for the H_{c+}^{out} scenario depicted in Fig. 10(d-f), ϵ_{in} remains again largely unaffected by these imaginary perturbations for the delocalized. However, for the delocalized ϵ_{out} , the imaginary perturbation in $\Im(k_m)$ significantly alters its delocalization pattern. Meanwhile, perturbations in

damping coefficient, respectively (Wu et al., 2023a; Chen et al., 2021b). This means that the transfer function H in real experiments may not always be real-valued and can carry non-negligible imaginary components. To account for these practical considerations, we introduce real-valued perturbations into the system parameters M and m in the form of $X_{\text{perturbation}} = \Re(X)$, and complex-valued perturbations into $k_{1,2,m}$ and H in the form of $X_{\text{perturbation}} = \Re(X) + i\Im(X)$. Fig. 9 illustrates corresponding eigenmodes for four types of real-valued random disorders ranging from 15% to 25%. As shown, both ϵ_{in} and ϵ_{out} , whether exhibiting delocalized or enhanced localization, retain their modal profiles with minor perturbations, indicating the robustness of the system. Fig. 10 demonstrates the impact of imaginary perturbations on the modal profiles of ϵ_{in} and ϵ_{out} at their respective delocalization transfer functions H_{c+}^{in} and H_{c+}^{out} . As shown in Fig. 10(a-c) for the case of H_{c+}^{in} , the delocalized ϵ_{in} and ϵ_{out} with enhanced localization remain largely unaffected by these imaginary perturbations, despite some minor local perturbations on the modal profiles. As for the H_{c+}^{out} scenario depicted in Fig. 10(d-f), ϵ_{in} remains again largely unaffected by these imaginary perturbations for the delocalized. However, for the delocalized ϵ_{out} , the imaginary perturbation in $\Im(k_m)$ significantly alters its delocalization pattern. Meanwhile, perturbations in

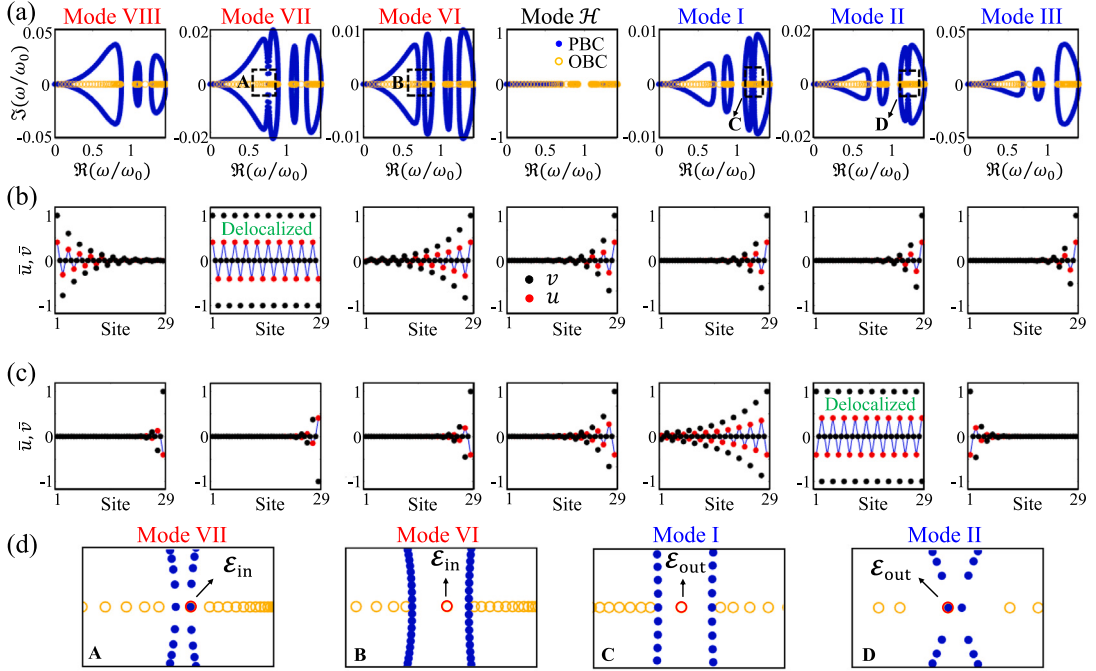


Fig. 8. H -dependent modal profiles of the TEMs in the non-Hermitian meta-lattices. (a) Comparison between the PBC and OBC spectra at the representative modes highlighted in Fig. 7(c) and (d), with $\delta k = -0.2$. Magnified views around the transition points at modes I, II, VI, and VII are presented in (d). (b) Spatial profiles of ϵ_{in} at the selected modes. (c) Spatial profiles of ϵ_{out} at the selected modes. The transfer functions for all the cases included read $H_{\mathcal{H}} = 0$, $H_I = 0.1$, $H_{II} = 0.145$, $H_{III} = 0.3$, $H_{VI} = -0.1$, $H_{VII} = -0.345$, and $H_{VIII} = -0.5$.

$\Im(H_{c+}^{\text{out}})$ and $\Im(k_{1,2})$ cause only minor distortions to the modal profile of ϵ_{out} . The numerical results displayed in both Figs. 9 and 10 are obtained after averaging over ten simulations.

To numerically demonstrate asymmetric TEM delocalization behavior, we conduct transient analysis for the non-Hermitian meta-lattice. The meta-lattice is excited with a narrow-band tone burst signal at the lattice center (the 16th lattice site). Fig. 11(a) and (b) show the time-dependent magnitudes of $|u|$, at representative H . When $H = 0$, the system is Hermitian, and only right-localized TEMs are observed, consistent with predictions from Fig. 8 for mode \mathcal{H} . As H decreases from 0 to -0.5 , ϵ_{in} undergoes delocalization at the critical $H_{c+}^{\text{in}} = -0.345$, followed by a TEM relocation at $H < -0.345$. During the transition process of ϵ_{in} , ϵ_{out} remains right-localized but with enhanced localization strength. Conversely, when increasing H from 0 to 0.3, ϵ_{in} stays right-localized with amplified localization, while ϵ_{out} experiences a delocalization at the critical $H_{c+}^{\text{out}} = 0.145$ and subsequently a relocation as H goes beyond. The transient results support the eigenmode analysis in Fig. 8 and demonstrate the asymmetric delocalization of the two TEMs caused by the NHSE. It is worth noting that in cases of ϵ_{in} at $H = 0.3$ and ϵ_{out} at $H = -0.5$, some fields with weak intensities are observed localized on the left edge of the meta-lattice. This is attributed to a non-zero H which inevitably narrows the bandwidths of both BSBGs, pushing $\epsilon_{\text{in,out}}$ close to the bulk skin modes localized to the left.

6. Morphing of topological edge modes in 1D and 2D non-Hermitian meta-lattices

The transformation of topological modes in 2D non-Hermitian topological systems include the dynamic evolution and control of TEMs under varying parameters, the influence of NHSE on TEM behaviors, and the potential for engineering adiabatic transitions and topological pumps. In this section, we will first investigate an elastic topological pump facilitated by the delocalization of TEMs through the dynamic tuning of H . Our focus will be on two main aspects: (1) We will present a computational demonstration of the temporal transformation of TEM, specifically a 1D temporal TEM pumping within a 1D non-Hermitian meta-lattice featuring a time-dependent $H(t)$. (2) Additionally, we will illustrate spatial TEM transformation, encompassing a spatial rendition of the temporal TEM pumping. This will occur within a 2D stacked non-Hermitian meta-lattice, subject to diverse evolutions of $H(y)$ along the y -direction.

The concept of 1D adiabatic topological pumping has been extensively explored in 1D active acoustic and mechanical systems utilizing electrical motors and shunted piezoelectric materials, enabling temporal edge-bulk-edge wave transport (Xu et al., 2020; Xia et al., 2021). In our study, we investigate an adiabatic temporal pumping involving the delocalization of TEMs within a finite non-Hermitian meta-lattice depicted in Fig. 12(a). The meta-lattice is modulated by a time-varying transfer function $H(t) = H_0 + H_m \cos(\omega_m t + \phi_m)$, where $H_0 = -0.25$, $H_m = -0.15$, $\omega_m = \omega_{\text{in}}/150$, and $\phi_m = \pi$. At $t = 0$, $H(0) = -0.1$ exceeds the critical

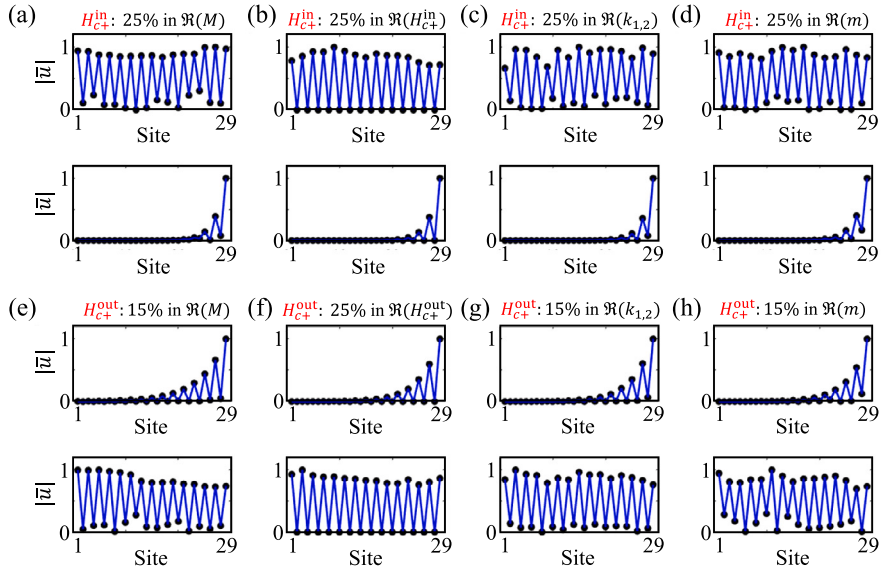


Fig. 9. Normalized magnitude profiles of outer mass displacement $|u|$ for E_{in} (top) and E_{out} (bottom) at critical delocalization transfer functions H_{c+} under various types of real-valued random disorders in the outer mass $\Re(M)$, critical transfer function $\Re(H_{c+})$, outer Hookean spring $\Re(k_{1,2})$, and inner mass $\Re(m)$ for the non-Hermitian meta-lattices presented in Fig. 6(a). Specifically, (a-d) show the delocalized E_{in} and the non-delocalized E_{out} with enhanced localization at $H_{c+}^{in} = -0.345$, whereas (e-h) show the delocalized E_{out} and the non-delocalized E_{in} with enhanced localization at $H_{c+}^{out} = 0.145$. The percentages are calculated relative to the unperturbed real-valued parameters.

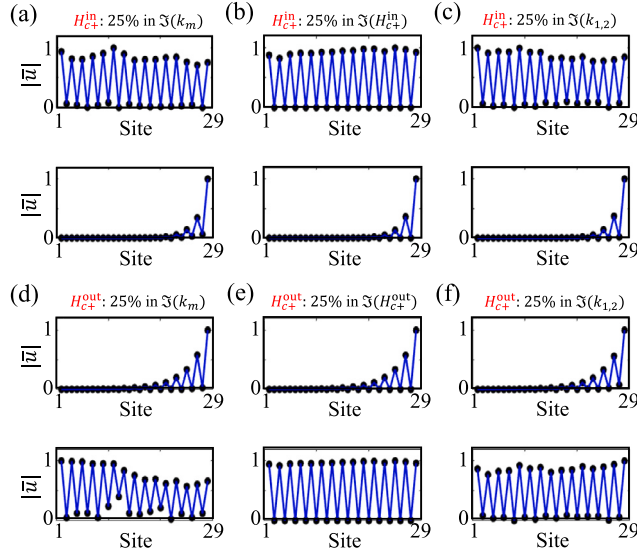


Fig. 10. Normalized magnitude profiles of outer mass displacement $|u|$ for E_{in} (top) and E_{out} (bottom) at critical delocalization transfer functions H_{c+} under various types of imaginary-valued random disorders in the inner Hookean spring $\Im(k_m)$, imaginary component of critical transfer function $\Im(H_{c+})$, and outer Hookean spring $\Im(k_{1,2})$ for the non-Hermitian meta-lattices presented in Fig. 6(a). Specifically, (a-c) show the delocalized E_{in} and the non-delocalized E_{out} with enhanced localization at $H_{c+}^{in} = -0.345$, whereas (d-f) show the delocalized E_{out} and the non-delocalized E_{in} with enhanced localization at $H_{c+}^{out} = 0.145$. The percentages are calculated relative to the unperturbed real-valued parameters.

$H_{c+}^{in} = -0.345$, and at $t = \pi/\omega_m$, $H(0) = -0.4$ falls below $H_{c+}^{in} = -0.345$. This implies an edge-extended-edge transition as t progresses from 0 to π/ω_m . Moreover, the modulation frequency $\omega_m \ll \omega_{in}$ ensures a slow modulation, corresponding to a sufficiently long modulation period for an adiabatic protocol (Zhu et al., 2021). To demonstrate the temporal TEM pumping, the temporal evolution of the spatial profile $|u|$ of outer masses M for E_{in} is shown in Fig. 12(b). The meta-lattice is excited at the rightmost site with an 80-cycle tone burst signal centered at $\omega_{in} = 0.76925\omega_0$. The entire simulation spans $300T_{in,out}$ corresponding to two edge-extended-edge pumping cycles, where $T_{in,out}$ denote the period for $E_{in,out}$. The change in field localization direction from left to right and back

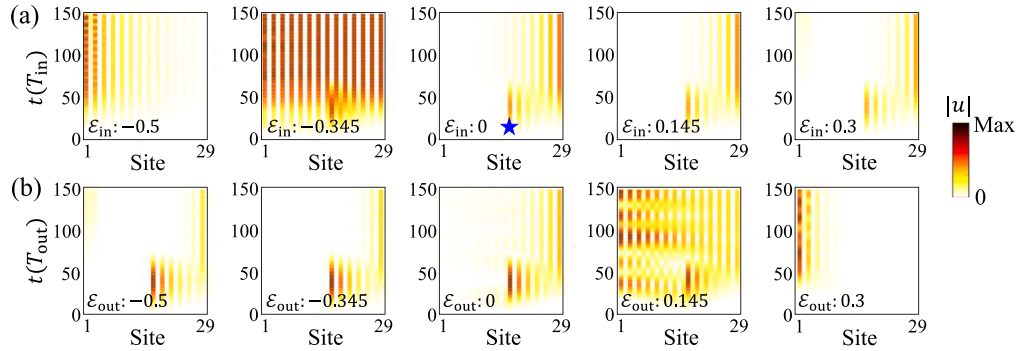


Fig. 11. Transient demonstration of the asymmetric delocalization of TEMs within the non-Hermitian meta-lattice. (a,b) Time-dependent displacement magnitudes $|u|$ for ε_{in} (a) and ε_{out} (b) at frequencies $\omega_{\text{in}} = 0.76925\omega_0$ and $\omega_{\text{out}} = 1.1189\omega_0$, respectively. The corresponding periods are $T_{\text{in},\text{out}} = 2\pi/\omega_{\text{in},\text{out}}$. Five different values of H are selected, including the critical transfer functions $H_{c+}^{\text{in},\text{out}}$. The tone burst excitation is applied at the center of the meta-lattice (marked in blue) and is described by $F(t) = \sin(\omega_{\text{in}/\text{out}}t)(1 - \cos(\omega_{\text{in}/\text{out}}t/80))$.

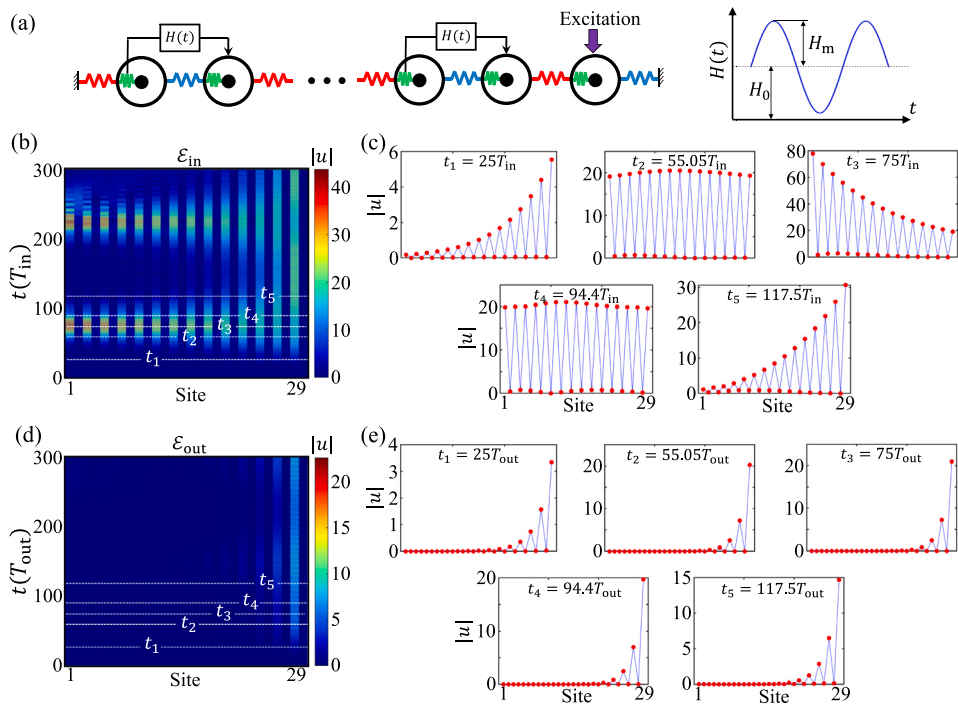


Fig. 12. Demonstration of the adiabatic temporal evolution in a temporally modulated non-Hermitian meta-lattice. (a) The meta-lattice consists of 15 unit cells with the leftmost site removed. An 80-cycle tone-burst excitation is applied to the rightmost site. The right panel shows the time-dependent profile of the time-varying transfer function $H(t)$. (b) The time-dependent magnitude profile of ε_{in} ($T_{\text{in}} = 2\pi/\omega_{\text{in}}$, $\omega_{\text{in}} = 0.76925\omega_0$). Five representative time instants are selected. (c) The magnitudes at the representative time instants, showing a complete pumping cycle for ε_{in} . (d) The time-dependent magnitude profile of ε_{out} ($T_{\text{out}} = 2\pi/\omega_{\text{out}}$, $\omega_{\text{out}} = 1.1189\omega_0$). Five representative time instants are selected. (e) The magnitudes at the representative time instants for ε_{out} . In (c) and (e), only the displacement magnitudes $|u|$ are displayed.

to left is evident as time progresses. To illustrate the temporal pumping more clearly, we select five representative time instants and examine the corresponding field profiles in Fig. 12(c). Transitions occur with a change in field localization direction, marked by the delocalization of TEMs, as seen at $t_2 = 55.05T$ and $t_4 = 94.4T$. In contrast, ε_{out} within the temporally modulated meta-lattice exhibits an opposite behavior, remaining localized on the right edge during the modulation, as shown in Fig. 12(d). The profiles of displacement magnitude $|u|$ for ε_{out} at the five selected time instants are shown in Fig. 12(e). Similarly, modulating $H(t)$ about the other critical transfer function $H_{c+}^{\text{out}} = 0.145$ results in temporal adiabatic pumping at ε_{out} , while ε_{in} exhibits enhanced right localization.

Synthetic dimensions emerge as a novel platform for exploring higher-dimensional topological systems and their associated physical phenomena that are not accessible to experiments in real spatial dimensions. With the help of synthetic dimensions,

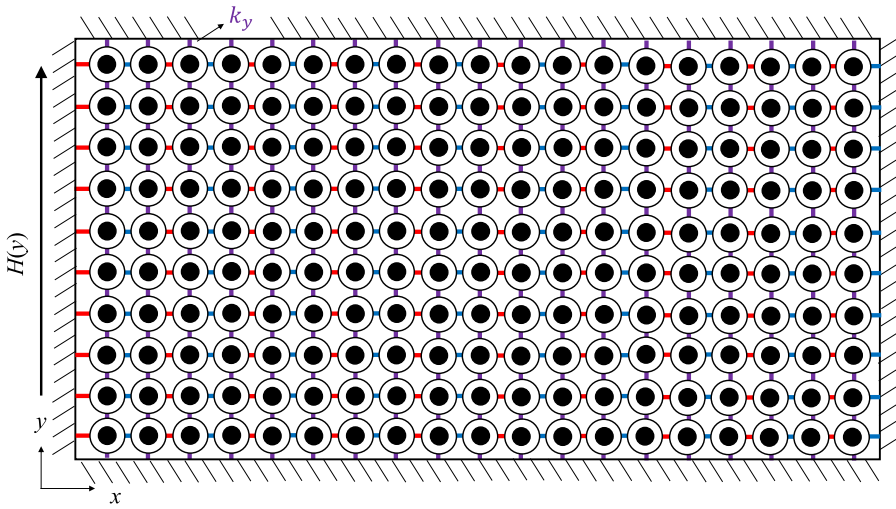


Fig. 13. Schematic of the 2D stacked meta-lattice comprising 10×19 sites for the demonstration of spatial morphing of the TEMs. y -dependent transfer functions $H(y)$ and coupling springs k_y connecting adjacent layers are illustrated. The 2D meta-lattice is grounded on the edges.

adiabatic topological pumping that emulates higher-dimensional quantum Hall effect has been experimentally observed for photonics, acoustics and even mechanics (Zilberman et al., 2018; Chen et al., 2021a; Wang et al., 2023c; Cheng et al., 2024). Very recently, inspired by the notion of synthetic dimension, a novel class of static mechanical topological insulators with discarded time dimension and enhanced spatial dimensions have been uncovered, promising potential applications in mechanical load filtering and insulation (Wang et al., 2023a,b).

To construct a synthetic time in this work, we map the temporal dimension t to a spatial dimension y . This mapping transforms $H(t)$ into $H(y)$, which evolves in the y -direction of a 2D stacked non-Hermitian meta-lattice, consisting of 19×10 sites and confined with fixed OBCs on the surrounding boundaries; see Fig. 13. The resulting 2D meta-lattice is essentially a stack of 1D non-Hermitian meta-lattices modulated by $H(y)$ and connected by interchain springs k_y along the y -direction. k_y controls the coupling between adjacent 1D non-Hermitian meta-lattices, with higher values narrowing and eventually closing the BSBGs. Typically, a spatial pumping phenomenon featuring an edge-extended-edge transition of TEM can occur by choosing an evolution of $H(y)$ that crosses one of the critical transfer functions (see also Appendix E for other 2D spatial morphing patterns of the TEMs enabled by different choices of $H(y)$). Due to the asymmetric delocalization of TEMs within the two BSBGs, the spatial pumping should occur only at either \mathcal{E}_{in} or \mathcal{E}_{out} , depending on which critical transfer functions $H(y)$ crosses. Taking \mathcal{E}_{out} as an example, to observe one cycle of the spatial pumping, we sweep $H(y)$ from 0 to 0.2 in the $+y$ direction (Fig. 14(a)) and select $k_y = 0.01$ as the weak coupling among each row to ensure the existence of distinguishable BSBGs. As shown in Fig. 14(b) and (c), the selected \mathcal{E}_{in} maintains its right localization, while the selected \mathcal{E}_{out} exhibits an edge-extended-edge transition (from the right to left edges) in the $+y$ -direction, as the evolution of $H(y)$ crosses the corresponding critical transfer function $H_{c+}^{\text{out}} = 0.145$, at which the delocalization of \mathcal{E}_{out} occurs. Similarly, in Fig. 14(d), $H(y)$ is chosen to sweep from -0.15 to -0.45 and to cross the corresponding $H_{c+}^{\text{in}} = -0.345$ for the delocalization of \mathcal{E}_{in} . As expected, Fig. 14(e) indicates an edge-extended-edge transition at \mathcal{E}_{in} . On the contrary, no transition is observed for \mathcal{E}_{out} , as shown in Fig. 14(f).

To demonstrate spatial TEM pumping, Fig. 15 presents the time-dependent spatial profiles for both \mathcal{E}_{in} and \mathcal{E}_{out} when taking different $H(y)$. In the transient simulations, the 2D lattice is excited at the bottom right with an 80-cycle tone burst signal centered at $\omega_{\text{in}} = 0.7709\omega_0$ for \mathcal{E}_{in} shown in Fig. 15(a) and (c) and $\omega_{\text{out}} = 1.1882\omega_0$ for \mathcal{E}_{out} shown in Fig. 15(b) and (d). The sampling frequency is set to $T_{\text{in,out}}/30$. As time progresses, the excitation of \mathcal{E}_{out} with $H(y)$ evolving from 0 to 0.2 is pumped from the bottom right to the top left through the delocalization; see Fig. 15(b). However, for the excitation of \mathcal{E}_{in} , the edge-extended-edge transition does not take place, and the time-dependent field profile always shows right localization; see Fig. 15(a). On the other hand, for the extended meta-lattice with $H(y)$ evolving from -0.15 to -0.45 , the transient profile of \mathcal{E}_{in} exhibits edge-extended-edge transition; see Fig. 15(c), while that of \mathcal{E}_{out} remains localized on the right, not showing pumping behavior; see Fig. 15(d). The transient simulation results agree well with the prediction of the eigenmode analysis given in Fig. 14, validating the asymmetric spatial pumping among the two TEMs. It is worth mentioning that even though there are only ten layers along y , which does not necessarily obey the adiabatic theorem, the 1D spatial topological pumping still works without evident coupling with other non-Hermitian skin modes in the bulk.

7. Conclusion

The impact of NHSE on the localization of in-gap TEMs is demonstrated in a 1D non-Hermitian topological meta-lattice. The discrete spring-mass meta-lattice is constructed with local resonance that creates two BSBGs with nontrivial topology and active

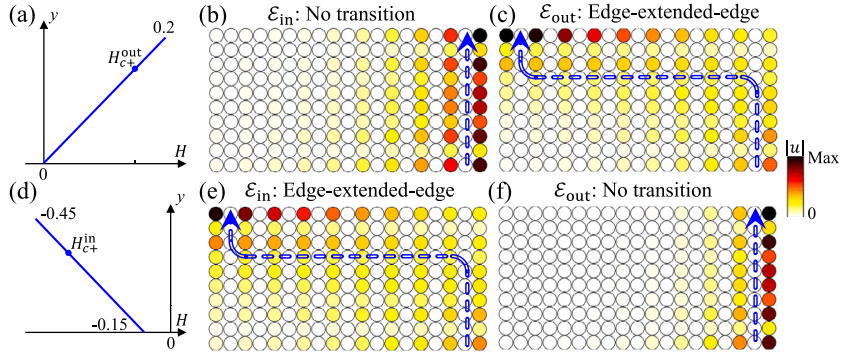


Fig. 14. Spatial TEM pumping in a 2D stacked non-Hermitian meta-lattice. (a) Illustration of $H(y)$ in function of y for spatial pumping of ϵ_{out} . (b,c) Modal profiles of (b) ϵ_{in} at $\omega_{\text{in}}/\omega_0 = 0.7709$ and (c) ϵ_{out} at $\omega_{\text{in}}/\omega_0 = 1.1882$ with $H(y)$ given in (a). (d) Illustration of $H(y)$ in function of y for spatial pumping of ϵ_{in} . (e,f) Modal profiles of (e) ϵ_{in} at $\omega_{\text{in}}/\omega_0 = 0.7709$ and (f) ϵ_{out} at $\omega_{\text{in}}/\omega_0 = 1.1882$ with $H(y)$ given in (d). In (b,c,e,f), only the displacement amplitudes of outer masses $|u|$ are presented, and the blue arrow lines correspond to the field evolution in $+y$.

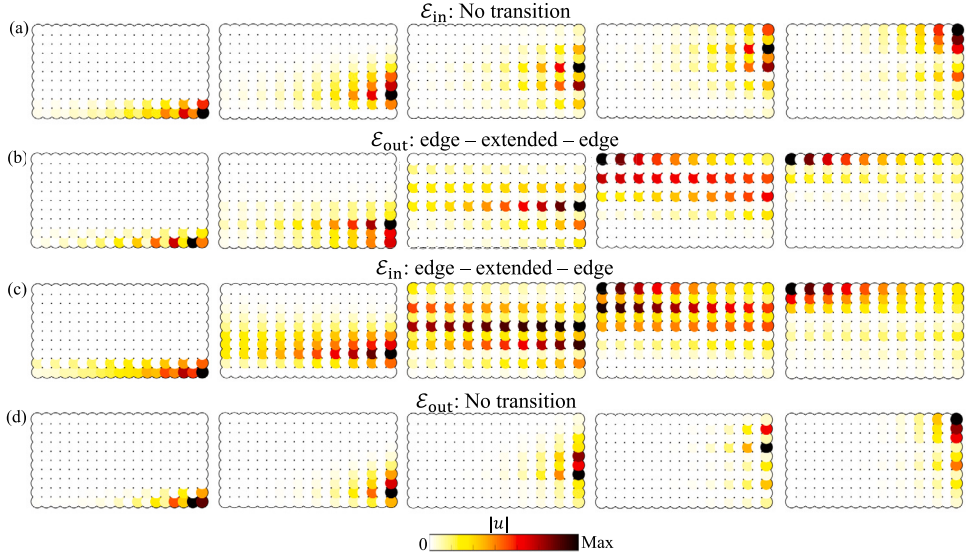


Fig. 15. Transient analysis of the 2D spatial TEM pumping in the 2D stacked non-Hermitian lattices. (a-d) Time-dependent displacement magnitude u of the four representative modes illustrated in Fig. 14. Five time instants are selected for all the cases. Only displacement magnitudes $|u|$ are displayed.

feedback control that induces system non-Hermiticity. To modify the localization of TEMs and delocalize them, we leverage the opposing localization tendencies by local resonance-based NHSE to counterbalance the original localization of TEMs. We propose using tunable feedback control to achieve asymmetric field localization caused by the NHSE within the vicinity of the two BSBGs. This asymmetry in field localization leads to the selective delocalization of the two TEMs at different control strengths or transfer functions, thereby achieving asymmetric TEM delocalization. We observe that the feedback control strengths required for this delocalization do not align with those needed for the emergence of exceptional points, unlike the reported scenarios (Zhu et al., 2021; Wang et al., 2023a). The asymmetric TEM delocalization behavior is numerically validated using finite-difference simulations. Furthermore, we investigate non-Hermitian temporal and spatial topological pumping in a 1D time-varying and a 2D stacked non-Hermitian meta-lattices. The spatial topological pumping can be treated as the 2D non-Hermitian morphing of TEMs and extended to various 2D wave patterns (Wang et al., 2022b). Note that the proposed discrete non-Hermitian meta-lattice, governed by Newton's law of motion, can be readily realizable in various types of physical systems, such as continuous piezoelectric-based structural beams and plates (see Fig. A.16 in Appendix A), as well as robotic metamaterials (Chen et al., 2021b; Brandenbourger et al., 2019). Overall, this work provides insight into manipulating the competition between TEM and non-Hermitian skin modes to control in-plane topological waves in both 1D and 2D mechanical systems.

CRediT authorship contribution statement

Qian Wu: Writing – review & editing, Writing – original draft, Validation, Methodology, Investigation, Formal analysis, Conceptualization. **Shaoyun Wang:** Writing – original draft, Investigation, Formal analysis. **Honghua Qian:** Formal analysis. **Yanzheng Wang:** Formal analysis. **Guoliang Huang:** Writing – review & editing, Validation, Supervision, Funding acquisition, Formal analysis, Conceptualization.

Declaration of competing interest

The authors declare that they have no known competing financial interests or personal relationships that could have appeared to influence the work reported in this paper.

Acknowledgments

This work is supported by the Air Force Office of Scientific Research under Grant No. AF 9550-18-1-0342 and AF 9550-20-1-0279 with Program Manager Dr. Byung-Lip (Les) Lee.

Appendix A. Physical realization of discrete non-Hermitian meta-lattices

Based on the design of our recent odd-mass metamaterials (Wu et al., 2023a), the spring-mass model in this study can be physically implemented using a one-dimensional PZT-based structured beam, where the dynamic response is governed by in-plane motions, as schematically shown in Fig. A.16(a). In this realization, the deformations of the springs $k_{1,2}$ in the discrete spring-mass model are represented by the stretching of the beams of different width, connecting adjacent outer masses, while k_m is achieved by the beams linking the outer and inner masses. The feedback controller with a transfer function H , connecting the PZT sensors and actuators, is illustrated schematically in Fig. A.16(b). The stretching deformation of the k_m beam induces bending in the vertical supporting beam (highlighted in green in Fig. A.16(a)), allowing the PZT sensor to detect the equivalent deformation of k_m . The detected signal is then processed through the controller and sent to the nearest-neighbor PZT actuator, effectively applying an external force that drives the horizontal motion of the outer mass M through another vertical supporting beam (highlighted in blue in Fig. A.16(a)). In Fig. A.16(c), the dispersion curves for eigenmodes only with longitudinal polarization is numerically calculated. The corresponding eigenmodes at the Brillouin zone boundaries are showcased in Fig. A.16(d). These results show qualitative agreement with those presented in Fig. 1(b).

Appendix B. Complex dispersion diagrams and energy consideration of non-Hermitian meta-lattices

As discussed in the main text, both the real and imaginary components of the complex PBC dispersion diagrams, $\Re(\omega/\omega_0)$ and $\Im(\omega/\omega_0)$, can be adjusted by manipulating H . As depicted in Fig. B.17, the increase in $|H|$ primarily amplifies the magnitude of $\Im(\omega/\omega_0)$, while noticeable alterations in $\Re(\omega/\omega_0)$ occur when $|H|$ reaches higher values. Across all scenarios illustrated in Fig. B.17, changing the sign of H effectively reverses the signs of all imaginary dispersion bands, thereby reversing the directions of wave amplification and attenuation.

The energetic gain and loss, reflecting the imaginary components of the dispersion diagram $\Im(\omega/\omega_0)$ shown in Fig. 2(c) and (e), can be explained using an energy-based approach. Assuming a cyclic protocol that defines $u_n^{1,2} = |u^{1,2}|e^{i(qn-\omega t+\phi_{1,2})}$, the total energy extracted over a cycle of oscillation is

$$\Delta W = \Re \left[\int_0^T \frac{\partial(u^1)^*}{\partial t} H e^{-iq}(u^2 - u^1) dt \right] = -\frac{2\pi\omega^2 H}{\omega_0^2 - \omega^2} |u^1| |u^2| \sin(\phi_1 - \phi_2 + q), \quad (\text{B.1})$$

where $T = 2\pi/\omega$ denotes the period. As can be seen, the sign of the total energy, $\text{sgn}(\Delta W)$, predicting the evolution of field magnitudes along certain directions depends on $\text{sgn}(H)$, $\omega_0^2 - \omega^2$, and $\phi_1 - \phi_2 + q$. Note that Eq. (B.1) provides a mechanistic insight into the wave-associated energy amplification and attenuation and reflects the imaginary components of eigenfrequencies $\Im(\omega/\omega_0)$. As shown in Fig. B.18(a), when $H > 0$, at $\omega < \omega_0$ (the lower two bands), the feedback control does negative/positive work ($\Delta W < 0/\Delta W > 0$) at $q > 0$ but positive/negative work ($\Delta W > 0/\Delta W < 0$) at $q < 0$ for the first/second band. However, at $\omega > \omega_0$ (the upper two bands), the feedback control does positive/negative work ($\Delta W > 0/\Delta W < 0$) at $q > 0$ but negative/positive work ($\Delta W < 0/\Delta W > 0$) at $q < 0$ for the third/fourth band. Specifically, positive/negative work corresponds to wave amplification/attenuation during propagation, also reflected by negative/positive $\Im(\omega/\omega_0)$ given in Fig. 2(c). As for $H = -0.2$, taking $H < 0$ simply swaps the signs of both $\Im(\omega/\omega_0)$ and ΔW for all the bands. In this case, the resulting wave amplification and attenuation directions are opposite in comparison with the $H = 0.2$ scenario, as depicted in Figs. 2(e) and B.18 (b).

To interpret the NHSE, in addition to the calculation of winding number nu , we can also solve the eigenvalue problems given by Eq. (13), leading to the characteristic equation

$$2k_0^2(1 + \cos q) + \omega^2 M_{\text{odd}} k_0(1 + e^{-iq}) - (2k_0 - \omega^2 M_{\text{eff}})^2 = 0. \quad (\text{B.2})$$

When ω lies only on the real axis, as depicted by the OBC spectra in Fig. 2(f) and (g), there are two solutions in the form of $q = \Re(q) + i\Im(q)$, due to the quadratic equation form for e^{iq} . While $\Re(q)$ constructs the real-valued band structure given in Fig. 2(b)

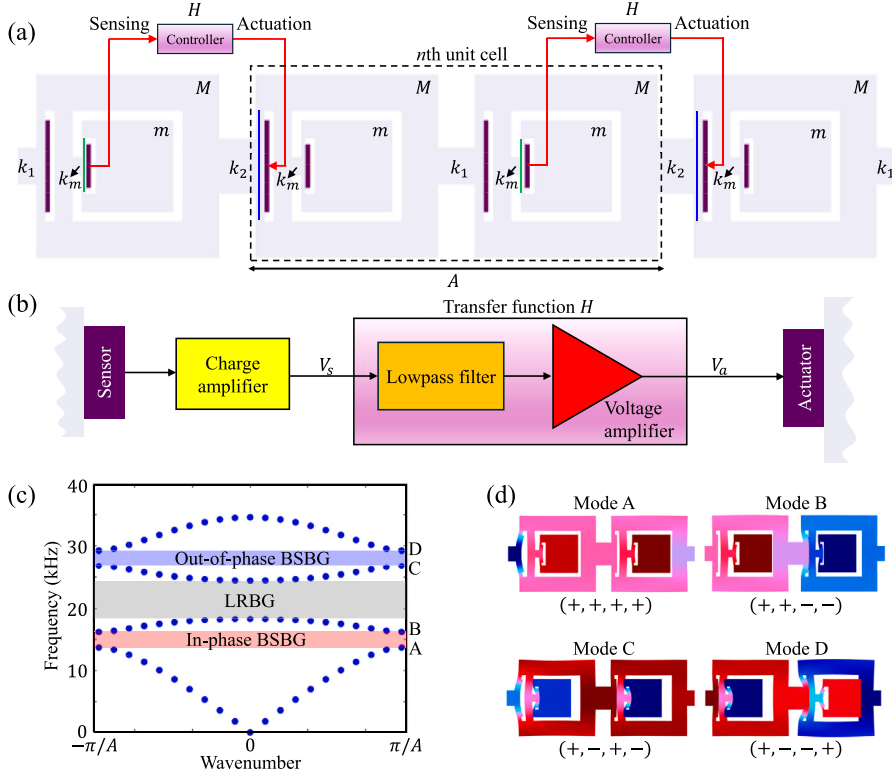


Fig. A.16. Potential physical realization of the non-Hermitian meta-lattice using structural beam system. (a) Continuous model equivalent to the discrete spring-mass system. PZT sensors (shorter purple bars) are connected to PZT actuators (longer purple bars) via feedback controllers with transfer functions H . The base material is steel, and the lattice constant $A = 24$ mm. (b) Schematic of the digital control system. Specifically, the nominator and the denominator of the transfer function $H(\omega) = H_0 / (\frac{\omega^2}{\omega_0^2} + \frac{i\eta\omega}{\omega_0} + 1)$ are realized, respectively, by the voltage amplifier and lowpass filter. ω_0 and η denote the cut-off frequency and damping coefficient, respectively. (c) Dispersion curves of the continuous model for longitudinal modes, showing two BRBGs separated by a LRBG. (d) The modal profiles of the four eigenmodes at the boundaries of the Brillouin zone are presented, with “+” and “-” denoting $+x$ and $-x$ modal deformations, respectively.

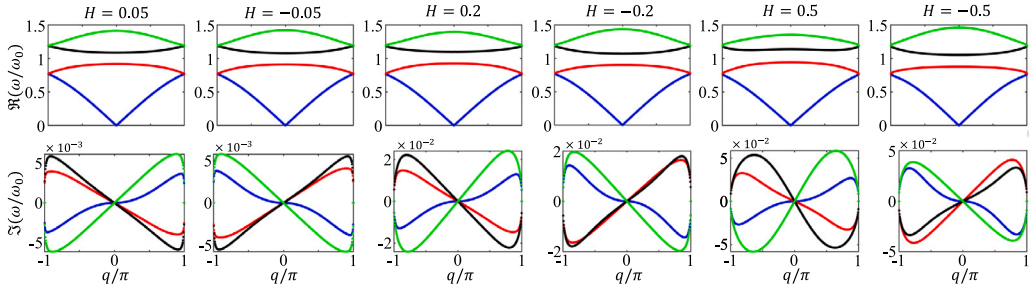


Fig. B.17. H -dependent complex dispersion diagram for the non-Hermitian meta-lattice under PBCs. Real $\Re(\omega/\omega_0)$ (top) and imaginary $\Im(\omega/\omega_0)$ (bottom) components of the complex PBC dispersion diagrams are presented for the meta-lattices illustrated in Fig. 2(a) when $H = 0.05$, $H = -0.05$, $H = 0.2$, $H = -0.2$, $H = 0.5$, and $H = -0.5$.

and (d), $\Im(q)$ indicates that the associated wave modes are spatially asymmetric, either exponentially amplified or attenuated towards one end. The calculated $\Im(q)$ for the non-Hermitian meta-lattice is plotted in Fig. B.18(c) and (d) for $H > 0$ and $H < 0$, respectively. Within the pass bands, $\Im(q)$ takes opposite signs across the LRBG, indicating that the localization direction of skin modes residing within the lower two bands opposes that of those residing within the upper two bands. This provides an intriguing explanation for the opposite field localization of the NHSE within the non-Hermitian meta-lattices.

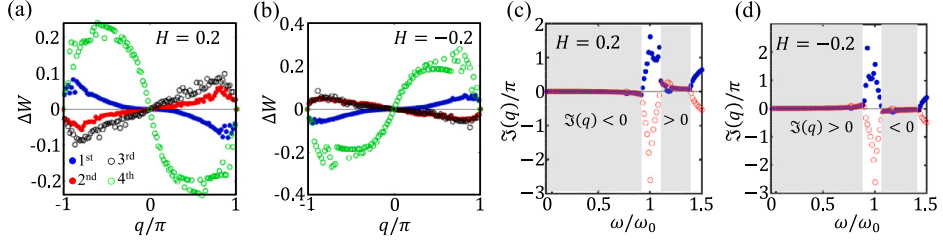


Fig. B.18. (a,b) The work done, ΔW , by H for each band shown in Fig. 2 is numerically calculated for $H = 0.2$ and $H = -0.2$. (c,d) The inverse decay length, $\mathcal{L}(q)$, is calculated when $H = 0.2$ and $H = -0.2$, based on Eq. (B.2).

Appendix C. Proof for the independence of ω_{TEM} on H

First, we rewrite the equations of motion given in Eq. (1) and the boundary conditions given in Eq. (18) of the N -unit-cell Hermitian ($H = 0$) meta-lattice with the removal of the leftmost site in the matrix form as

$$\omega^2 \mathbf{M}_0 \mathbf{u} = \mathbf{D}_0 \mathbf{u} \quad (\text{C.1})$$

where $\mathbf{u} = [u_1^2, v_1^2, u_2^1, u_2^2, v_2^1, v_2^2, \dots, u_N^1, u_N^2, v_N^1, v_N^2]^T$ whose length is $4N - 2$, and \mathbf{M}_0 and \mathbf{D}_0 are the mass and stiffness matrices which read

$$\mathbf{M}_0 = \begin{bmatrix} M & 0 & 0 & 0 & 0 & 0 & \dots & 0 & 0 & 0 & 0 \\ 0 & m & 0 & 0 & 0 & 0 & \dots & 0 & 0 & 0 & 0 \\ 0 & 0 & M & 0 & 0 & 0 & \dots & 0 & 0 & 0 & 0 \\ 0 & 0 & 0 & M & 0 & 0 & \dots & 0 & 0 & 0 & 0 \\ 0 & 0 & 0 & 0 & m & 0 & \dots & 0 & 0 & 0 & 0 \\ 0 & 0 & 0 & 0 & 0 & m & \dots & 0 & 0 & 0 & 0 \\ \vdots & \vdots & \vdots & \vdots & \vdots & \ddots & \vdots & \vdots & \vdots & \vdots & \vdots \\ 0 & 0 & 0 & 0 & 0 & 0 & \dots & M & 0 & 0 & 0 \\ 0 & 0 & 0 & 0 & 0 & 0 & \dots & 0 & M & 0 & 0 \\ 0 & 0 & 0 & 0 & 0 & 0 & \dots & 0 & 0 & m & 0 \\ 0 & 0 & 0 & 0 & 0 & 0 & \dots & 0 & 0 & 0 & m \end{bmatrix}, \quad (\text{C.2})$$

and

$$\mathbf{D}_0 = \begin{bmatrix} k_1 + k_m & -k_m & 0 & 0 & 0 & 0 & \dots & 0 & 0 & 0 & 0 \\ -k_m & k_m & 0 & 0 & 0 & 0 & \dots & 0 & 0 & 0 & 0 \\ -k_2 & 0 & k_t & -k_1 & -k_m & 0 & \dots & 0 & 0 & 0 & 0 \\ 0 & 0 & -k_1 & k_t & 0 & -k_m & \dots & 0 & 0 & 0 & 0 \\ 0 & 0 & -k_m & 0 & k_m & 0 & \dots & 0 & 0 & 0 & 0 \\ 0 & 0 & 0 & -k_m & 0 & k_m & \dots & 0 & 0 & 0 & 0 \\ \vdots & \vdots & \vdots & \vdots & \vdots & \ddots & \vdots & \vdots & \vdots & \vdots & \vdots \\ 0 & 0 & 0 & 0 & 0 & 0 & \dots & k_t & -k_1 & -k_m & 0 \\ 0 & 0 & 0 & 0 & 0 & 0 & \dots & -k_1 & k_t & 0 & -k_m \\ 0 & 0 & 0 & 0 & 0 & 0 & \dots & -k_m & 0 & k_m & 0 \\ 0 & 0 & 0 & 0 & 0 & 0 & \dots & 0 & -k_m & 0 & k_m \end{bmatrix}, \quad (\text{C.3})$$

respectively. Eq. (C.1) can be recast into

$$\omega^2 \mathbf{u} = \mathcal{H}_0 \mathbf{u}, \quad (\text{C.4})$$

with $\mathcal{H}_0 = \mathbf{M}_0^{-\frac{1}{2}} \mathbf{D}_0 \mathbf{M}_0^{-\frac{1}{2}}$. When $H \neq 0$, the meta-lattice is non-Hermitian, and Eq. (C.4) can be modified accordingly as

$$\omega^2 \mathbf{u} = [\mathcal{H}_0 + \delta \mathcal{H}(H)] \mathbf{u}. \quad (\text{C.5})$$

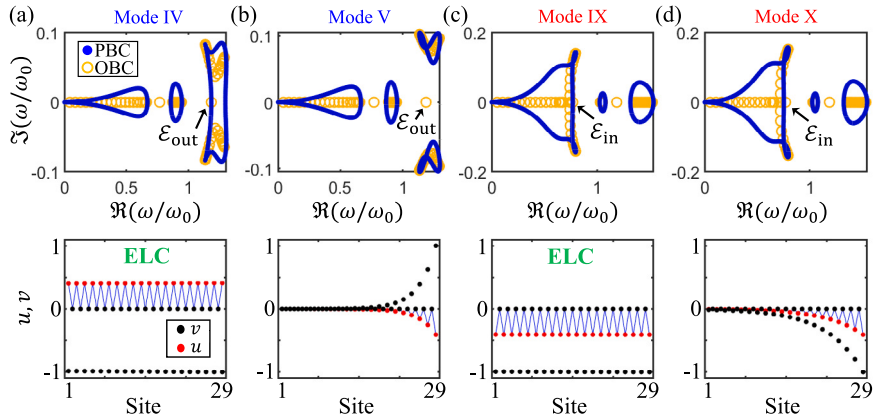


Fig. C.19. Asymmetric phase transition in the open non-Hermitian lattice. (a–b) Comparison between the OBC and PBC spectra (top) and the corresponding modal profiles (bottom) of the TEM modes selected in Fig. 7(c) and (d). the ELCs are highlighted.

where

$$\delta\mathcal{H} = \begin{bmatrix} 0 & 0 & 0 & 0 & 0 & 0 & 0 & \dots & 0 & 0 & 0 & 0 & 0 & 0 & 0 & 0 & 0 \\ 0 & 0 & 0 & 0 & 0 & 0 & 0 & \dots & 0 & 0 & 0 & 0 & 0 & 0 & 0 & 0 & 0 \\ \frac{H}{M} & \frac{-H}{\sqrt{Mm}} & 0 & 0 & 0 & 0 & 0 & \dots & 0 & 0 & 0 & 0 & 0 & 0 & 0 & 0 & 0 \\ 0 & 0 & 0 & 0 & 0 & 0 & 0 & \dots & 0 & 0 & 0 & 0 & 0 & 0 & 0 & 0 & 0 \\ 0 & 0 & 0 & 0 & 0 & 0 & 0 & \dots & 0 & 0 & 0 & 0 & 0 & 0 & 0 & 0 & 0 \\ 0 & 0 & 0 & 0 & 0 & 0 & 0 & \dots & 0 & 0 & 0 & 0 & 0 & 0 & 0 & 0 & 0 \\ 0 & 0 & 0 & \frac{H}{M} & 0 & \frac{-H}{\sqrt{Mm}} & 0 & \dots & 0 & 0 & 0 & 0 & 0 & 0 & 0 & 0 & 0 \\ \vdots & \vdots & \vdots & \vdots & \vdots & \vdots & \ddots & \vdots \\ 0 & 0 & 0 & 0 & 0 & 0 & 0 & \dots & 0 & 0 & 0 & 0 & 0 & 0 & 0 & 0 & 0 \\ 0 & 0 & 0 & 0 & 0 & 0 & 0 & \dots & 0 & 0 & 0 & 0 & 0 & 0 & 0 & 0 & 0 \\ 0 & 0 & 0 & 0 & 0 & 0 & 0 & \dots & 0 & 0 & 0 & 0 & 0 & 0 & 0 & 0 & 0 \\ 0 & 0 & 0 & 0 & 0 & 0 & 0 & \dots & \frac{H}{M} & 0 & \frac{-H}{\sqrt{Mm}} & 0 & 0 & 0 & 0 & 0 \\ 0 & 0 & 0 & 0 & 0 & 0 & 0 & \dots & 0 & 0 & 0 & 0 & 0 & 0 & 0 & 0 & 0 \\ 0 & 0 & 0 & 0 & 0 & 0 & 0 & \dots & 0 & 0 & 0 & 0 & 0 & 0 & 0 & 0 & 0 \\ 0 & 0 & 0 & 0 & 0 & 0 & 0 & \dots & 0 & 0 & 0 & 0 & 0 & 0 & 0 & 0 & 0 \end{bmatrix}. \quad (\text{C.6})$$

We diagonalize Eq. (C.5) as

$$\omega^2 \mathbf{v} = (\boldsymbol{\Lambda} + \boldsymbol{\Delta}) \mathbf{v}, \quad (\text{C.7})$$

where $\boldsymbol{\Delta} = \mathbf{U}_0^T \delta\mathcal{H} \mathbf{U}_0$, $\mathbf{v} = \mathbf{U}_0^T \mathbf{u}$, and $\boldsymbol{\Lambda}$ and \mathbf{U}_0 are formed by the eigenvalues and column eigenvectors of \mathcal{H}_0 (Strang, 2016). We assumed the k th eigenvector of \mathcal{H}_0 corresponds to the right-localized TEM whose modal profile is described by Eq. (20). In Eq. (20), we observe that this right-localized TEM eigenvector follows a field pattern of

$$\mathbf{U}_{0,k} = [u_1^{2R}, v_1^{2R}, 0, u_2^{2R}, 0, v_2^{2R}, \dots, 0, u_N^{2R}, 0, v_N^{2R}]^T. \quad (\text{C.8})$$

Now, we prove that the k th row in $\boldsymbol{\Delta}$ vanishes. The element on the k th row and j th column in matrix $\boldsymbol{\Delta}$ reads

$$\Delta_{kj} = U_{0,kp} \delta\mathcal{H}_{pq} U_{0,qj} = 0, \quad (\text{C.9})$$

because $U_{0,kp} \delta\mathcal{H}_{pq} = 0$ can be proved readily by observing the pattern of Eqs. (C.8) and (C.6). In Eq. (C.9), it is important to note that the indices j, p, q range from $1, 2, 3, \dots, 4N - 2$. Additionally, the Einstein summation convention is applied in this context. As a consequence of the vanishment of k th row in Δ_{kj} , k th Geršgorin disc $R_k = \sum_j |\Delta_{jk}|$ is 0 and it is reduced to a point. The eigenvalue with $H = 0$ is located at the point, so it cannot escape this point with $H \neq 0$ because of the Geršgorin disc theorem (Horn and Johnson, 2012). Consequently, the eigenfrequency of the non-Hermitian system proposed in this work consistently equals the eigenfrequency of its Hermitian counterpart, regardless of H . It can be proved using an alternative approach as shown in the following. The eigenvalue is the root of the determinant

$$\det(\mathbf{A}) = 0. \quad (\text{C.10})$$

where $\mathbf{A} = \omega^2 \mathbf{I} - \Delta - \Delta$, and \mathbf{I} is the identity matrix. Because the k th row of Δ is equal to $\mathbf{0}$, the determinant has the following form

$$\det \begin{bmatrix} A_{1,1} & \dots & A_{1,k-1} & A_{1,k} & A_{1,k+1} & \dots & A_{1,4N-2} \\ \vdots & & \vdots & \vdots & \vdots & & \vdots \\ A_{k-1,1} & \dots & A_{k-1,k-1} & A_{k-1,k} & A_{k-1,k+1} & \dots & A_{k-1,4N-2} \\ 0 & \dots & 0 & \omega^2 - \omega_{\text{TEM}}^2 & 0 & \dots & 0 \\ A_{k+1,1} & \dots & A_{k+1,k-1} & A_{k+1,k} & A_{k+1,k+1} & \dots & A_{k+1,4N-2} \\ \vdots & & \vdots & \vdots & \vdots & & \vdots \\ A_{4N-2,1} & \dots & A_{4N-2,k-1} & A_{4N-2,k} & A_{4N-2,k+1} & \dots & A_{4N-2,4N-2} \end{bmatrix}. \quad (\text{C.11})$$

According to the Laplace expansion along the k th row, the determinant reads

$$\begin{aligned} \det(\mathbf{A}) &= 0C_{1,k} + 0C_{2,k} + \dots + (\omega^2 - \omega_{\text{TEM}}^2)C_{k,k} + \dots + 0C_{4N-2,k} \\ &= (\omega^2 - \omega_{\text{TEM}}^2)C_{k,k} \\ &= 0, \end{aligned} \quad (\text{C.12})$$

where $C_{i,j}$ is the (i, j) -cofactor of matrix \mathbf{A} , and it is generally non-zero. Therefore, we have $\omega = \omega_{\text{TEM}}$, thus proving the proposition that the eigenfrequency of a TEM in a non-Hermitian system equals that of its Hermitian counterpart. Moreover, this conclusion remains correct when the rightmost site is removed instead of the leftmost site. In this case, the k th column in Δ is equal to $\mathbf{0}$, and the Laplace expansion along the k th column gives $\omega = \omega_{\text{TEM}}$.

Appendix D. Asymmetric phase transition by non-Hermitian skin effect

As discussed previously in Fig. 8, as $H < 0$ decreases from $H = 0$, only the lower two bands undergo phase transitions: the in-phase BSBG experiences closing, re-opening, and re-closing. In contrast, the upper two bands remain as two isolated loops with the survival of the out-of-phase BSBG. As $H > 0$ increases from $H = 0$, the upper two bands undergo the phase transitions whereas the lower two bands remain as two isolated loops with the survival of the in-phase BSBG. The spatial profiles of ε_{in} and ε_{out} around the first symmetric TEM delocalization have been examined in Fig. 8. Here, we delve into the details of how the NHSE impacts the TEMs gapped within the two BSBGs after the second phase transition, namely at H_c^- . Fig. C.19 compares the OBC and PBC spectra in the complex domain for modes IV, V, IX, and X highlighted in Fig. 7(c) and (d), along with their respective modal profiles clearly visualizing the field localization. The OBC spectra are obtained for the non-Hermitian meta-lattice depicted in Fig. 6(a). As shown in Fig. C.19(a), at H_c^{out} , the delocalization of ε_{out} is observed, due to that ω_{out} now falls exactly on the left ($q = 0$) of the PBC loop, causing $u_n^{1,2} = u_{n+1}^{1,2}$ and $v_n^{1,2} = v_{n+1}^{1,2}$. In other words, the out-of-phase oscillations of both M and m occur only on one of the two sides of the equilibrium axis. More interestingly, it is seen from Fig. 7(c) that the delocalized ε_{out} is fully embedded within the bulk bands, which are all NHSE-induced skin modes localized to the left edge. This makes ε_{out} an extended bound state in a localized continuum (ELC), which has been recently investigated experimentally in 2D higher-order topological insulators with non-Hermiticity (Wang et al., 2022a). Later, when H reaches $H = 0.9$ at mode V, the formed PBC loop splits into two isolated PBC loops residing symmetrically with respect to the real axis $\Im\omega/\omega_0 = 0$, and ε_{out} is relocalized back to the right see Fig. C.19(b). This is because ω_{out} is no longer encircled by the PBC loop and hence is not affected by the localization of NHSE and shows the same localization direction as mode H. On the other hand, at the second phase transition $H_c^{\text{in}} = -1.725$, ω_{in} falls on the right edge ($q = 0$) of the PBC loop formed by the lower two bands, featuring a modal profile of $u_n^{1,2} = u_{n+1}^{1,2}$ and $v_n^{1,2} = v_{n+1}^{1,2}$. Similar to ω_{out} given in Fig. C.19(a), M and m oscillate in-phase only on one of the two sides of the equilibrium axis; see Fig. C.19(c). As H increases to $H = -1.9$, ω_{in} relocates back to the right since ω_{in} is no longer encircled by the PBC loop of the lower two bands and hence is not affected by the localization of NHSE; see Fig. C.19(d).

As demonstrated in Figs. 8 and C.19, the phase transition featuring the delocalization of TEMs does not necessarily coincide with the emergence of exceptional points on PBC spectra. As shown in Figs. 8(d), C.19(a), and (c), ε_{in} and ε_{out} become perfectly delocalized at the critical transfer functions, when they fall exactly on the associated PBC spectral loop, while exceptional points have not yet formed. These critical transfer functions represent the critical NHSE strengths that cancel the field localization of TEMs. This is understandable in the context of the purely real-valued system investigated here. Due to the use of purely real transfer functions H , if $\omega_{\text{in,out}}$ are real, their corresponding eigenfunctions must also be real-valued. For a delocalized TEM, we have $u_n^{1,2} = \pm u_{n+1}^{1,2}$ and $v_n^{1,2} = \pm v_{n+1}^{1,2}$. This is equivalent to the PBC conditions $u_{n+1}^{1,2} = u_n^{1,2} e^{iq}$ and $v_{n+1}^{1,2} = v_n^{1,2} e^{iq}$, where q is 0 or π . This further indicates that $\varepsilon_{\text{in,out}}$ must fall spectrally on either $q = 0$ or $q = \pi$, corresponding to the intersections of the PBC loops with the real axis $\Im(\omega/\omega_0) = 0$. Furthermore, these transitions can also be seen as topological transitions, characterized by the jump of the winding number v with respect to the eigenfrequencies of the concerned TEMs. Recalling Eq. (14), one can calculate the winding number v in the complex- ω domain for non-Hermitian systems. Here, we emphasize that v not only predicts the existence and the localization direction of NHSE but also measures the competition between NHSE and TEMs (Zhu et al., 2021). When $v \neq 0$, NHSE overpowers TEM in terms of the localization strength, and the localization direction aligns with that of NHSE. When $v = 0$, NHSE is weaker, and the localization direction coincides with that of TEM. At the critical H_c , v is ill-defined, and TEMs are perfectly delocalized.

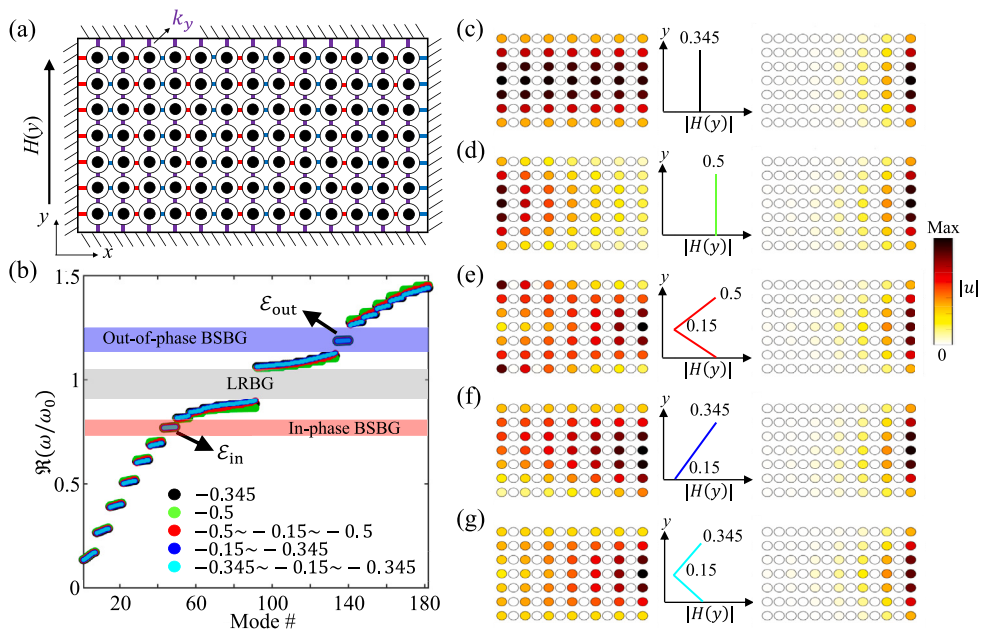


Fig. D.20. $H(y)$ -dependent non-Hermitian morphing of the TEMs in the 2D stacked non-Hermitian meta-lattice illustrated in Fig. 14(a). (a) Schematic of the meta-lattice including 7×13 sites. y -dependent transfer functions $H(y)$ and coupling springs $k_y = 0.01$ which connect adjacent layers are also illustrated. The meta-lattice is grounded on the edges. (b) The real part of the complex frequency spectra of the meta-lattice with selected $H(y)$. Here, only negative $H(y)$ is considered, which corresponds to the delocalization and relocalization of \mathcal{E}_{in} . Both \mathcal{E}_{in} and \mathcal{E}_{out} are marked by the black arrows. $k_y = 0.01$ is considered for weak interactions among adjacent layers. (c–g) The modal profiles of \mathcal{E}_{in} at $\omega = 0.7734\omega_0$ (left) and \mathcal{E}_{out} at $\omega = 1.1894\omega_0$ (right). The distributions of $H(y)$ are indicated in the middle. In the figures showing field profiles, only the displacements of outer masses $|u|$ are presented.

Appendix E. Other non-Hermitian spatial morphing patterns of topological edge modes

In Fig. 14, we discussed the spatial TEM pumping. Additionally, tuning $H(y)$ allows for other spatial morphing patterns of TEMs (Wang et al., 2022b). As shown in Fig. D.20(b), while modifying $H(y)$ alters the eigenfrequencies of bulk modes, those of the TEMs remain unchanged. Within each of the BSBGs, there are seven TEMs due to the y -directional sizes of the extended meta-lattice. Numerical eigenmode analyses reveal five representative morphed modes activated by specific $H(y)$, demonstrating distinct morphing behaviors (Fig. D.20(c–g)). Throughout these scenarios, $H(y) < 0$ implies that \mathcal{E}_{out} consistently remains right-localized (see the right panel of Fig. D.20(c–g)). Meanwhile, the modal profile of selected \mathcal{E}_{in} is morphed based on the y -directional evolution of $H(y)$ (see the left panel of Fig. D.20(c–g)).

Data availability

Data will be made available on request.

References

- Chiu, C.-K., Teo, J.C., Schnyder, A.P., Ryu, S., 2016. Classification of topological quantum matter with symmetries. *Rev. Modern Phys.* 88 (3), 035005.
- Arfken, G.B., Weber, H.J., Harris, F.E., 2011. *Mathematical Methods for Physicists: a Comprehensive Guide*. Academic Press.
- Ni, X., Yves, S., Krasnok, A., Alù, A., 2023. Topological metamaterials. *Chem. Rev.*
- Ma, G., Xiao, M., Chan, C.T., 2019. Topological phases in acoustic and mechanical systems. *Nat. Rev. Phys.* 1 (4), 281–294.
- Lu, L., Joannopoulos, J.D., Soljačić, M., 2014. Topological photonics. *Nat. Photonics* 8 (11), 821–829.
- He, C., Ni, X., Ge, H., Sun, X.-C., Chen, Y.-B., Lu, M.-H., Liu, X.-P., Chen, Y.-F., 2016. Acoustic topological insulator and robust one-way sound transport. *Nature Phys.* 12 (12), 1124–1129.
- Fan, H., Xia, B., Tong, L., Zheng, S., Yu, D., 2019. Elastic higher-order topological insulator with topologically protected corner states. *Phys. Rev. Lett.* 122 (20), 204301.
- Klitzing, K.v., Dorda, G., Pepper, M., 1980. New method for high-accuracy determination of the fine-structure constant based on quantized Hall resistance. *Phys. Rev. Lett.* 45 (6), 494.
- T Thouless, D.J., Kohmoto, M., Nightingale, M.P., den Nijs, M., 1982. Quantized Hall conductance in a two-dimensional periodic potential. *Phys. Rev. Lett.* 49 (6), 405.
- Kunst, F.K., Edvardsson, E., Budich, J.C., Bergholtz, E.J., 2018. Biorthogonal bulk-boundary correspondence in non-Hermitian systems. *Phys. Rev. Lett.* 121 (2), 026808.
- Yang, Z., Zhang, K., Fang, C., Hu, J., 2020. Non-Hermitian bulk-boundary correspondence and auxiliary generalized Brillouin zone theory. *Phys. Rev. Lett.* 125 (22), 226402.

- Ghatak, A., Brandenbourger, M., Van Wezel, J., Coulais, C., 2020. Observation of non-Hermitian topology and its bulk-edge correspondence in an active mechanical metamaterial. *Proc. Natl. Acad. Sci.* 117 (47), 29561–29568.
- Ashida, Y., Gong, Z., Ueda, M., 2020. Non-hermitian physics. *Adv. Phys.* 69 (3), 249–435.
- Bergholtz, E.J., Budich, J.C., Kunst, F.K., 2021. Exceptional topology of non-hermitian systems. *Rev. Modern Phys.* 93 (1), 015005.
- Okuma, N., Kawabata, K., Shiozaki, K., Sato, M., 2020. Topological origin of non-Hermitian skin effects. *Phys. Rev. Lett.* 124 (8), 086801.
- Leykam, D., Bliokh, K.Y., Huang, C., Chong, Y.D., Nori, F., 2017. Edge modes, degeneracies, and topological numbers in non-Hermitian systems. *Phys. Rev. Lett.* 118 (4), 040401.
- He, Y., Chien, C.-C., 2020. Non-hermitian generalizations of extended Su-Schrieffer-Heeger models. *J. Phys.: Condens. Matter.* 33 (8), 085501.
- Gong, Z., Ashida, Y., Kawabata, K., Takasan, K., Higashikawa, S., Ueda, M., 2018. Topological phases of non-Hermitian systems. *Phys. Rev. X* 8 (3), 031079.
- Ding, K., Fang, C., Ma, G., 2022. Non-Hermitian topology and exceptional-point geometries. *Nat. Rev. Phys.* 4 (12), 745–760.
- Huang, H., Sun, C., 2009. Wave attenuation mechanism in an acoustic metamaterial with negative effective mass density. *New J. Phys.* 11 (1), 013003.
- Wu, Z., Xia, R., Yi, J., Li, Z., 2023b. Multiple topological interface modes in electromechanically resonant piezoelectric beams. *Eng. Struct.* 281, 115716.
- Wang, W., Wang, X., Ma, G., 2022b. Non-Hermitian morphing of topological modes. *Nature* 608, 50.
- Zhu, W., Teo, W.X., Li, L., Gong, J., 2021. Delocalization of topological edge states. *Phys. Rev. B* 103 (19), 195414.
- Wu, Q., Zhang, X., Shivashankar, P., Chen, Y., Huang, G., 2022. Independent flexural wave frequency conversion by a linear active metalayer. *Phys. Rev. Lett.* 128 (24), 244301.
- Wu, Q., Xu, X., Qian, H., Wang, S., Zhu, R., Yan, Z., Ma, H., Chen, Y., Huang, G., 2023a. Active metamaterials for realizing odd mass density. *Proc. Natl. Acad. Sci.* 120 (21), e2209829120.
- Chen, Y., Li, X., Scheibner, C., Vitelli, V., Huang, G., 2021b. Realization of active metamaterials with odd micropolar elasticity. *Nature Commun.* 12 (1), 1–12.
- Yi, J., Ma, Z., Xia, R., Negahban, M., Chen, C., Li, Z., 2022. Structural periodicity dependent scattering behavior in parity-time symmetric elastic metamaterials. *Phys. Rev. B* 106 (1), 014303.
- Zhao, D., Xiao, M., Ling, C.W., Chan, C.T., Fung, K.H., 2018. Topological interface modes in local resonant acoustic systems. *Phys. Rev. B* 98 (1), 014110.
- Liu, Z., Zhang, X., Mao, Y., Zhu, Y., Yang, Z., Chan, C.T., Sheng, P., 2000. Locally resonant sonic materials. *Science* 289 (5485), 1734–1736.
- Asbóth, J.K., Oroszlány, L., Pályi, A., 2016. A short course on topological insulators. *Lecture Notes Phys.* 919, 166.
- Scheibner, C., Souslov, A., Banerjee, D., Suriwka, P., Irvine, W., Vitelli, V., 2020. Odd elasticity. *Nat. Phys.* 16 (4), 475–480.
- Zhang, K., Yang, Z., Fang, C., 2020. Correspondence between winding numbers and skin modes in non-Hermitian systems. *Phys. Rev. Lett.* 125 (12), 126402.
- Wang, Y., Wu, Q., Tian, Y., Huang, G., 2024. Non-Hermitian wave dynamics of odd plates: Microstructure design and theoretical modelling. *J. Mech. Phys. Solids* 182, 105462.
- Yao, S., Wang, Z., 2018. Edge states and topological invariants of non-Hermitian systems. *Phys. Rev. Lett.* 121 (8), 086803.
- Yokomizo, K., Murakami, S., 2019. Non-bloch band theory of non-Hermitian systems. *Phys. Rev. Lett.* 123 (6), 066404.
- Mehri-Dehnavi, H., Mostafazadeh, A., 2008. Geometric phase for non-hermitian Hamiltonians and its holonomy interpretation. *J. Math. Phys.* 49 (8), 082105.
- Zhang, Q., Wu, B., et al., 2019. Non-Hermitian quantum systems and their geometric phases. *Phys. Rev. A* 99 (3), 032121.
- Xu, X., Wu, Q., Chen, H., Nassar, H., Chen, Y., Norris, A., Haberman, M.R., Huang, G., 2020. Physical observation of a robust acoustic pumping in waveguides with dynamic boundary. *Phys. Rev. Lett.* 125 (25), 253901.
- Xia, Y., Riva, E., Rosa, M.I., Cazzulani, G., Erturk, A., Braghin, F., Ruzzene, M., 2021. Experimental observation of temporal pumping in electromechanical waveguides. *Phys. Rev. Lett.* 126 (9), 095501.
- Zilberman, O., Huang, S., Guglielmon, J., Wang, M., Chen, K.P., Kraus, Y.E., Rechtsman, M.C., 2018. Photonic topological boundary pumping as a probe of 4D quantum Hall physics. *Nature* 553 (7686), 59–62.
- Chen, H., Zhang, H., Wu, Q., Huang, Y., Nguyen, H., Prodan, E., Zhou, X., Huang, G., 2021a. Creating synthetic spaces for higher-order topological sound transport. *Nature Commun.* 12 (1), 5028.
- Wang, S., Hu, Z., Wu, Q., Chen, H., Prodan, E., Zhu, R., Huang, G., 2023c. Smart patterning for topological pumping of elastic surface waves. *Sci. Adv.* 9 (30), eadh431.
- Cheng, W., Zhang, H., Wei, Y., Wang, K., Hu, G., 2024. Elastic energy and polarization transport through spatial modulation. *J. Mech. Phys. Solids* 182, 105475.
- Wang, A., Meng, Z., Chen, C.Q., 2023a. Non-Hermitian topology in static mechanical metamaterials. *Sci. Adv.* 9 (27), eadif7299.
- Wang, A., Zhou, Y., Chen, C.Q., 2023b. Topological mechanics beyond wave dynamics. *J. Mech. Phys. Solids* 173, 105197.
- Brandenbourger, M., Locsin, X., Lerner, E., Coulais, C., 2019. Non-reciprocal robotic metamaterials. *Nature Commun.* 10 (1), 1–8.
- Strang, G., 2016. Introduction to Linear Algebra. Wellesley.
- Horn, R., Johnson, C., 2012. Matrix Analysis. Cambridge University Press.
- Wang, W., Wang, X., Ma, G., 2022a. Extended state in a localized continuum. *Phys. Rev. Lett.* 129 (26), 264301.